HOLISMOKES – II. Identifying galaxy-scale strong gravitational lenses in Pan-STARRS using convolutional neural networks

R. Cañameras[1], S. Schuldt[1,2], S. H. Suyu[1,2,3], S. Taubenberger[1], T. Meinhardt[4], L. Leal-Taixé[4], C. Lemon[5], K. Rojas[5], E. Savary[5]

(Affiliations can be found after the references)

ABSTRACT

We present a systematic search for wide-separation (with Einstein radius $\theta_E \gtrsim 1.5''$), galaxy-scale strong lenses in the $30\,000\ \text{deg}^2$ of the Pan-STARRS 3π survey on the Northern sky. With long time delays of a few days to weeks, such systems are particularly well suited for catching strongly lensed supernovae with spatially-resolved multiple images and open new perspectives on early-phase supernova spectroscopy and cosmography. We produce a set of realistic simulations by painting lensed COSMOS sources on Pan-STARRS image cutouts of lens luminous red galaxies (LRGs) with known redshift and velocity dispersion from SDSS. First of all, we compute the photometry of mock lenses in *gri* bands and apply a simple catalog-level neural network to identify a sample of $1\,050\,207$ galaxies with similar colors and magnitudes as the mocks. Secondly, we train a convolutional neural network (CNN) on Pan-STARRS *gri* image cutouts to classify this sample and obtain sets of $105\,760$ and $12\,382$ lens candidates with scores $p_{CNN} > 0.5$ and > 0.9, respectively. Extensive tests show that CNN performances rely heavily on the design of lens simulations and choice of negative examples for training, but little on the network architecture. The CNN correctly classifies 14 out of 16 test lenses, which are previously confirmed lens systems above the detection limit of Pan-STARRS. Finally, we visually inspect all galaxies with $p_{CNN} > 0.9$ to assemble a final set of 330 high-quality newly-discovered lens candidates while recovering 23 published systems. For a subset, SDSS spectroscopy on the lens central regions proves our method correctly identifies lens LRGs at $z \sim 0.1$–0.7. Five spectra also show robust signatures of high-redshift background sources and Pan-STARRS imaging confirms one of them as a quadruply-imaged red source at $z_s = 1.185$ (likely a recently quenched galaxy) strongly lensed by a foreground LRG at $z_d = 0.3155$. In the future, high-resolution imaging and/or spectroscopic follow-up will be required to validate Pan-STARRS lens candidates and derive strong lensing models. We also expect that the efficient and automated two-step classification method presented in this paper will be applicable to the ∼4 mag deeper *gri* stacks from the Rubin Observatory Legacy Survey of Space and Time (LSST) with minor adjustments.

Key words. gravitational lensing: strong – data analysis: methods

1. Introduction

Strongly lensed systems with time-variable sources provide competitive probes of the Hubble constant H_0 that are independent from CMB observations (Planck Collaboration 2018) and the local distance ladder (Riess et al. 2019; Freedman et al. 2019, 2020), and allow one to assess the significance of the current H_0 tension. The H0LiCOW and COSMOGRAIL projects (e.g., Suyu et al. 2017; Courbin et al. 2018) have recently established the capacity of combining time-delay measurements and robust strong lensing models to constrain H_0, and measured $H_0 = 73.3^{+1.7}_{-1.8}$ km s^{-1} Mpc^{-1} in flat ΛCDM cosmology using six lensed quasars (Wong et al. 2019). The seventh lens has been analysed by the STRIDES collaboration (Shajib et al. 2020; Buckley-Geer et al. 2020), and a detailed study of systematic effects is presented by Millon et al. (2019) as part of the TDCOSMO organisation. Moreover, the first two strongly lensed supernovae (SNe) with spatially-resolved multiple images have been detected in recent years, one core-collapse SN behind the strong lensing cluster MACS J1149.5+222.3 (SN Refsdal, Kelly et al. 2015), and one type Ia SN behind an isolated lens galaxy (iPTF16geu, Goobar et al. 2017). These findings open a promising window for future H_0 measurements with lensed SNe. Such systems are indeed well suited for time-delay measurements given the smooth, non-erratic SNe light curves which require shorter high-cadence monitoring than lensed quasars, and the possibility to reduce microlensing ef-

fects by focusing on the early, achromatic expansion phase a few weeks after explosion, and by using color light curves (Suyu et al. 2020; Huber et al. 2019; Bonvin et al. 2019; Goldstein et al. 2018, Huber et al., 2020, in prep.;). For lensed type Ia SNe, the standardizable intrinsic peak luminosity of the source is also a valuable input for breaking the mass-sheet degeneracy in lens mass models (Falco et al. 1985). Constraints on H_0 have already been derived with SN Refsdal (Grillo et al. 2018, 2020) and illustrate the great potential of such measurements, in particular for galaxy-scale strong lens systems that have simpler lens mass distributions than galaxy clusters. Lensed SNe with adequate image separations providing time delays of a few days to weeks are particularly promising and are relatively less sensitive to microlensing effects (Suyu et al. 2020; Huber et al. 2019).

Besides precise measurements of the Hubble constant, strongly lensed SNe open an interesting window on early-phase SN studies. Multiply-imaged SNe detected from the first image can be combined with strong lensing models to predict the time delays and future SN reappearance (as was done for SN Refsdal) in order to trigger follow-up observations within a few days of explosion, which is currently not feasible for unlensed SNe beyond the local universe due to their late discovery near peak luminosity. Such early-phase studies are particularly valuable to tackle the progenitor problem of type Ia SNe and disentangle the single-degenerate (Whelan & Iben 1973), double-degenerate (Tutukov & Yungelson 1981), and additional scenarios that have

been extensively debated over the last decades. For core-collapse SNe, these observations are important to characterize the progenitor properties and compare with current stellar evolution models. Early-phase spectroscopy of type II SNe would yield novel constraints on the mass-loss history just before explosion.

We recently initiated the Highly Optimised Lensing Investigations of Supernovae, Microlensing Objects, and Kinematics of Ellipticals and Spirals (HOLISMOKES, Suyu et al. 2020) programme to address these fundamental questions on stellar physics and cosmology. The number of strongly lensed SNe is expected to grow over the next few years, thanks to the on-going Zwicky Transient Facility (ZTF, Masci et al. 2019) high-cadence survey on the northern hemisphere and the forthcoming Rubin Observatory Legacy Survey of Space and Time (LSST, Ivezić et al. 2019) on the south. Oguri & Marshall (2010) predict 45 strongly lensed type Ia SNe over the 10 years of LSST, which corresponds to a few events for the shallower ZTF survey. This assumes a selection from spatially-resolved multiple images targeting the most useful wide-separation systems. Using complementary selection techniques solely based on magnification of SN Ia light curves, Goldstein & Nugent (2017) predict 10 to 20 times more lensed SN Ia albeit mostly with small image separations (see also Wojtak et al. 2019). Importantly, new lensed SNe candidates have to be selected early enough to start the follow-up sequence in a timely manner. One way is to extend the numerous, successful searches of galaxy-scale strong lenses that were traditionally conducted on surveys with optimal image quality (e.g. More et al. 2016; Sonnenfeld et al. 2018), to surveys with largest sky coverage, in order to quickly identify transients matching the position of background lensed sources. Ultimately, these lens finding pipelines will be directly applicable to the deep LSST stacks which are expected to yield approximately a hundred thousand new systems (Collett 2015).

Galaxy-scale strong gravitational lenses without time-variable sources also provide valuable insights into the lens total mass distributions, including the inner dark-matter fractions (e.g., Gavazzi et al. 2007; Grillo et al. 2009; Sonnenfeld et al. 2015; Schuldt et al. 2019), the slopes of the total and dark-matter mass density profiles (e.g., Treu & Koopmans 2002; Koopmans et al. 2009; Barnabè et al. 2011; Shu et al. 2015), and the spatial extent of dark-matter halos (e.g., Halkola et al. 2007; Suyu & Halkola 2010). Such systems play a crucial role in characterizing the lens stellar initial mass function (IMF), a major ingredient for stellar mass estimates, as a function of galaxy physical properties (e.g., Cañameras et al. 2017b; Barnabè et al. 2013; Sonnenfeld et al. 2019), and they are well-suited to search for dark-matter substructures (e.g., Vegetti et al. 2012; Hezaveh et al. 2016; Ritondale et al. 2019). Moreover, high magnification factors provide unique diagnostics on the local interstellar medium physical conditions in lensed high-redshift galaxies and on the local feedback mechanisms driving their evolution (e.g., Danielson et al. 2011; Cañameras et al. 2017a; Cava et al. 2018).

Strong lensing events are rare, about 1 in 1000 for high-resolution space-based imaging (e.g., Marshall et al. 2009) and down to about 1 in 10^5 for seeing-limited ground-based data (e.g., Jacobs et al. 2019a), and their identification thus requires dedicated and automated methods. For instance, arc-finder algorithms (e.g., Gavazzi et al. 2014; Sonnenfeld et al. 2018) and citizen-science classification projects (Space Warps, Marshall et al. 2016) have been developed over the last decade. In particular, convolutional neural networks (CNNs) are supervised machine-learning algorithms optimized to image analysis (LeCun et al. 1998) that have proven to outperform other classification techniques and that require little pre-processing. They

are very efficient to peer into large imaging data sets and have been increasingly used in the field of astronomy over the last five years. These studies have established the ability of CNNs in recognizing galaxy morphologies (Dieleman et al. 2015), including the key features of strong gravitational lenses (Metcalf et al. 2019). Several CNN searches for new strong lens candidates have focused on ground-based imaging data, from the CFHTLS (Jacobs et al. 2017), KiDS DR3 (Petrillo et al. 2017) and DR4 (Petrillo et al. 2019; Li et al. 2020), DES Year 3 (Jacobs et al. 2019b,a), or the DESI DECam Legacy survey (Huang et al. 2019). Efficient classification pipelines using deep neural networks have also been developed and tested on simulated Euclid and LSST images to prepare for these forthcoming surveys which will tremendously increase the number of detectable strong lensing systems (Lanusse et al. 2018; Schaefer et al. 2018; Davies et al. 2019; Cheng et al. 2019; Avestruz et al. 2019).

In the meantime, no systematic searches of galaxy-galaxy strong lenses have so far taken advantage of the Pan-STARRS imaging covering the entire Northern sky. With this survey, Berghea et al. (2017) identified a strongly lensed QSO forming a quadruple system by cross-matching the position of a variable AGN selected in the mid-infrared. More recently, Rusu et al. (2019) performed a more systematic search of lensed QSOs by applying color/magnitude cuts and visually inspecting Pan-STARRS image cutouts of AGN candidates from the Wide-field Infrared Survey Explorer (Secrest et al. 2015). In this paper, we perform a comprehensive search for galaxy-scale strong lensing systems with luminous red galaxies (LRGs) as deflectors and typical high-redshift galaxies as background sources, using the extended footprint of nearly $30\,000$ deg^2 of the Pan-STARRS 3π survey on the Northern sky. The automated pipeline, based on a catalog-level pre-selection of galaxies and a convolutional neural network, results in a ranked list of candidates which we further inspect visually to select those with higher confidence for spectroscopic follow-up.

The outline of the paper is as follows. In Sect. 2 and 3, we give a short overview of the Pan-STARRS surveys and the overall search methodology and, in Sect. 4, we describe the simulation of strong lenses. In Sect. 5, we present the networks and training processes, and we extensively test the CNN performance. In Sect. 6 we finally apply the CNN to pre-selected Pan-STARRS image cutouts, provide the list of strong lens candidates from visual inspection, and characterize their overall properties. Our main conclusions appear in Sect. 7. Throughout this work, we adopt the flat concordant ΛCDM cosmology with $\Omega_M = 0.308$, and $\Omega_\Lambda = 1 - \Omega_M$ (Planck Collaboration XIII 2016), and with $H_0 = 72$ km s^{-1} Mpc^{-1} (Bonvin et al. 2017).

2. The Pan-STARRS1 survey

The Pan-STARRS1 (PS1) surveys were conducted with a 7 deg^2 field-of-view camera mounted on a 1.8 m telescope near the Haleakala summit, Hawaii, in the five broadband *grizy* SDSS-like filters (Chambers et al. 2016). The camera has a pixel size of 0.258$''$ pix^{-1} (Tonry & Onaka 2009). PS1 includes both the 3π and Medium Deep surveys. The former was completed in 2014 and made publicly available in DR1 and DR2. It covers $30\,000$ deg^2 on the Northern sky down to –30 deg in the five *grizy* filters with a depth of 21–23 mag. The median seeing FWHM is 1.31$''$, 1.19$''$, and 1.11$''$ in *g*, *r*, and *i* bands, respectively, but reaches >1.60$''$, >1.45$''$, and >1.35$''$ over 20% of the footprint (Chambers et al. 2016). The Medium Deep survey consists of 10 fields covering a total of 70 deg^2, with multiple visits in five filters optimized for transient detection. The few
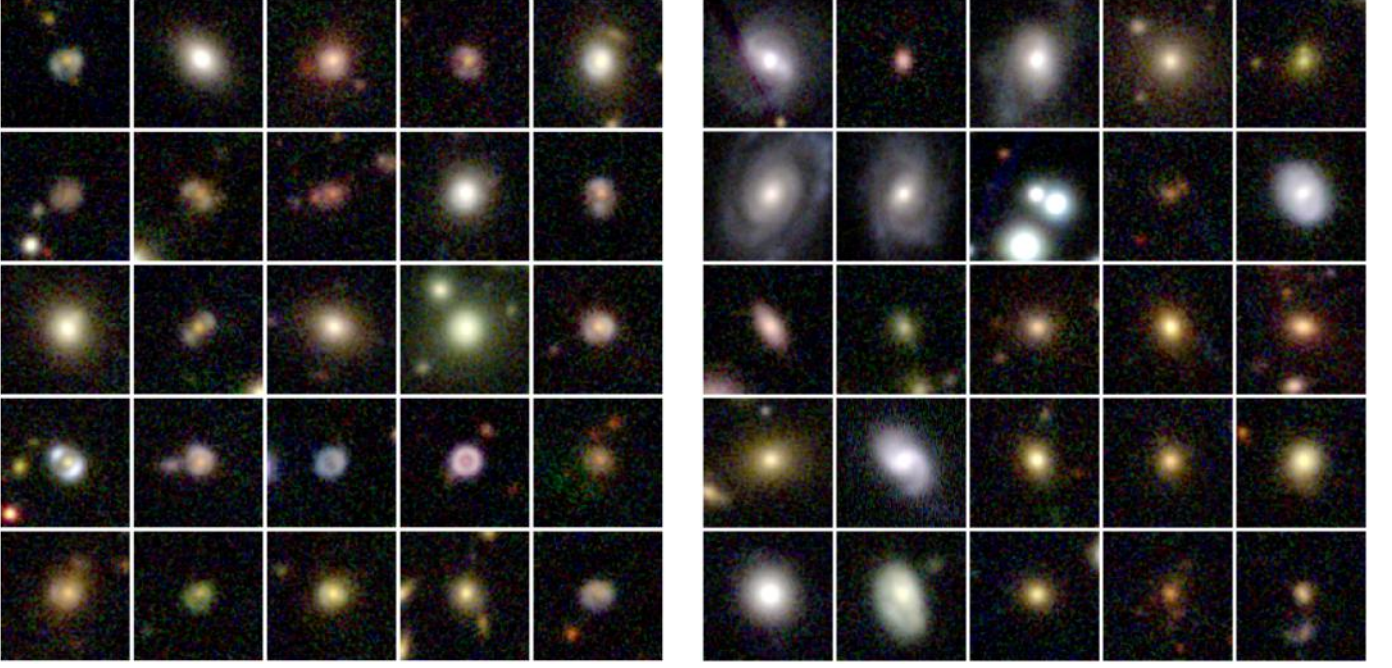
Fig. 1. *Left:* Examples of strong gravitational lens systems mocked up by painting COSMOS lensed sources on PS1 stack images, and used as positive examples for training. *Right:* PS1 postage stamps of a subset of the 90 000 galaxies used as negative examples, including face-on spirals, massive LRGs, and field galaxies with similar *gri* colors as the mocks. All postage stamps are $20'' \times 20''$.

hundred exposures will eventually provide deep stacks with 5σ point source detection limits down to $i \sim 26.0$ mag and will be available in the next data release (DR3).

We performed our search on the entire Northern sky with the 3π survey that overlaps nicely with on-going optical time-domain surveys on the Northern hemisphere (e.g., ZTF, Masci et al. 2019) which provide a wealth of astronomical transients, including strongly-lensed SNe. PS1 extends the SDSS to lower declinations and achieves higher depth. In particular, we apply our pipeline to *gri* stack images from DR1 which provide the optimal coaddition of individual exposures and have higher 5σ point-source sensitivities than z and y, probing down to 23.3, 23.2, and 23.1 mag in g, r, and i, respectively (Chambers et al. 2016). These three bands conveniently span a wavelength range sensitive to young stellar populations in blue star-forming galaxies at $z \gtrsim 1$ and to more dust-obscured or evolved early-type galaxies. Although the overall survey strategy provided limited variations in depth and image quality over large scales, 3π images have non uniform coverage on small scales due to the stacking process. We found that limiting magnitudes vary by up to ~0.5 mag on PS1 cutouts over the extragalactic sky and accounted for this effect in our analysis.

3. Overview of the lens-search method

In this paper, we aim at identifying galaxy-scale strong lensing systems on the extragalactic sky covered by PS1. We focus our search on typical high-redshift galaxies strongly lensed by massive LRGs, which have a higher lensing cross-section (Turner et al. 1984) and smooth light profiles that help separate the foreground and background emissions. In particular, given the long standing difficulty in distinguishing strong lensing features from arms of low redshift spirals, lenticular galaxies, tidal tails and other contaminants with arc-like features (e.g., Huang et al. 2019; Jacobs et al. 2019a), restricting to lens LRGs increases our

chance of robustly identifying multiple lensed images with the $> 1''$ average PSF FWHM of PS1.

Selecting these rare systems on the entire Northern sky requires an efficient analysis of the properties of the 3 billion sources detected in the PS1 3π survey image stacks. To circumvent memory limitations, a number of CNN searches in the literature have focused on subsets of galaxies with LRG-like photometry using, for instance, the Baryon Oscillation Spectroscopic Survey (BOSS) sample (Schlegel et al. 2009; Dawson et al. 2013) or dedicated color/magnitude *gri* cuts adapted from Eisenstein et al. (2001). However, this approach requires low contamination from lensed images to the lens multi-band photometry and was essentially applied to deeper surveys with better image quality (sub-arsec PSF FWHM in optical bands) than Pan-STARRS, such as the Hyper Suprime-Cam Subaru Strategic Program (HSC-SSP, Aihara et al. 2018; Sonnenfeld et al. 2018) or the Kilo-Degree Survey with OmegaCAM on the VLT Survey Telescope (KiDS, de Jong et al. 2013; Petrillo et al. 2019). Due to the lower image quality, applying such simple cuts on the photometry tabulated in Pan-STARRS DR2 catalogs would exclude significant fractions of interesting systems with strongly lensed arcs blended with the lens and altering its photometry. We therefore adopt a two-step approach: (1) a catalog-based neural network classification of source photometry, (2) a CNN trained on *gri* image cutouts.

In addition, we aim at finding wide-separation lens systems because these configurations provide longer time delays of a few days to weeks between multiple images, which is crucial to measure accurate, microlensing-free time delays for cosmology (Huber et al. 2019). Recently, the extensive follow-up of the lensed Type Ia SN iPTF16geu at $z = 0.4$ with $\theta_E \sim 0.3''$ (Goobar et al. 2017) illustrated the difficulty in reaching the time-delay precision required for cosmography on small-separation systems ($\Delta t < 2$ days, Dhawan et al. 2020), and demonstrated the impact of microlensing (More et al. 2017; Yahalomi et al. 2017; Bonvin et al. 2019). Focusing on wide separations is an effective search

strategy for the Pan-STARRS survey with limited angular resolution, and will help triggering timely imaging and spectroscopic follow-up.

As further described in Sect. 5, CNNs capture image characteristics by learning the coefficients of convolutional filters (kernels) of given width and height and creating a range of feature maps. They are invariant to translation and rotation. During the learning phase, the CNNs rely on training sets with representative labelled images to minimize the difference between predictions and ground truth. Classification algorithms require training sets of a few 10^4 to a million of labelled images depending on the number of classes, image complexity and network depth. In contrast to the recent computer vision image recognition challenges using deep CNNs (e.g., Russakovsky et al. 2015), relatively modest training sets of few 10^5 examples are sufficient for our two-class problem applied to small, galaxy-scale image cutouts (e.g., Jacobs et al. 2017, 2019a). Nonetheless, the small number and heterogeneous properties of spectroscopically-confirmed strong lenses (see the MasterLens database) make it necessary to use simulated systems.

Generating realistic mocks that account for the complexity of PS1 stack images is a critical ingredient to reach optimal classification performances (e.g., Lanusse et al. 2018). We construct our mocks by *painting* lensed arcs on PS1 *gri* images of LRGs with known redshift and velocity dispersion from SDSS spectroscopy. This approach captures the 3π survey properties, such as background artifacts, the presence of line-of-sight neighbouring galaxies, and local variations of seeing FWHM, exposure time and noise levels, while also accounting for variations in individual bands. In contrast to fully-simulated images, using real cutouts also guarantees positive examples that best mimic the small scale background properties inherited from the complex masking and stacking of individual PS1 exposures. As background sources, we use representative high-redshift galaxies from the COSMOS field. High S/N image cutouts are taken from HSC-SSP and Hubble Space Telescope (HST) to simulate lens distortions and magnifications, and we use *gri* bands (similar filter set as PS1) to provide color information.

In Sect. 4, we present the selection of lens and source galaxies and the pipeline to produce a set of mocks. Our first catalog-level network, described in Sect. 5.2, is trained on the multiband photometry of mocks and non-lens systems from the PS1 catalog, and assigns an output score, p_{cat}, ranging between 0 and 1. A much lower fraction of sources with $p_{cat} > 0.5$ are then classified with the CNN presented in Sect. 5.3, resulting in the final score, p_{CNN}. We eventually examine visually all sources with highest scores to assign grades and collect a list of high-confidence candidates for future validation.

4. Simulating galaxy-scale strong lenses

4.1. Selection of lens galaxies

Realistic strong lensing simulations require knowledge on the lens mass distribution and redshift. We therefore draw our sample of lens LRGs from the SDSS spectroscopic samples with reliable velocity dispersion measurements, to have a proxy of the lens total mass. We use the SDSS large scale structure catalogs of galaxies and QSOs for cosmological studies, including LOWZ and CMASS samples for BOSS (from SDSS DR12), and the higher-redshift LRG catalog for eBOSS (from SDSS DR14, Bautista et al. 2018). QSOs are excluded using SDSS `class` flag. This results in a broad sample of LRGs selected for their redder rest-frame colors using *gri* color/magnitude cuts

(Eisenstein et al. 2001). The sample is volume limited up to $z \sim 0.4$ (LOWZ), with additionally more luminous LRGs in the range $0.4 < z < 0.7$ (CMASS). eBOSS LRGs lie at higher redshift ($z_{med} \sim 0.7$, Prakash et al. 2016) due to a combination of optical/mid-infrared cuts in SDSS and WISE bands.

We clean this spectroscopic catalog to keep LRGs with reliable velocity dispersions, using $v_{disp} \leq 500$ km s^{-1} and $v_{disp,err} \leq 100$ km s^{-1}, and obtain 1 192 472 LRGs to build the mocks. We then cross-match with the PS1 catalog to obtain their photometry, image depth and seeing FWHM in PS1.

4.2. Selection of background sources

The sample of galaxies used to mock up high redshift lensed sources is drawn from the COSMOS field to take advantage of the wealth of existing data including ultra-deep optical imaging, multiband photometry, spectroscopic follow-up, and morphological classification. We select galaxies with morphological information from Galaxy Zoo: HST (Willett et al. 2017) and within the COSMOS2015 photometric catalog (Laigle et al. 2016) that also lists physical parameters from SED fitting. The former is a citizen science project that extends the original Galaxy Zoo (Lintott et al. 2008, 2011; Willett et al. 2013) with a thorough visual classification of galaxies with ACS imaging from the Hubble legacy surveys (see Scoville et al. 2007; Koekemoer et al. 2007, for the COSMOS field). In particular for COSMOS, Galaxy Zoo: HST relies on 3-color images obtained by combining the HST F814W mosaic with color gradients from ground-based imaging[1].

We clean the resulting catalog from sources identified as stars or artifacts (COSMOS2015 flag or visual identification), and remove very extended galaxies with $R_{eff} > 1.5''$, as well as galaxies contaminated by emission from companions within $5''$, and brighter by 1 mag in *r* band (Laigle et al. 2016). The output sample includes 52 696 galaxies for the strong lensing simulations. Redshifts are taken from public spectroscopic redshift catalogs drawn from surveys with VLT/VIMOS (zCOSMOS-bright, Lilly et al. 2007), VLT/FORS2 (Comparat et al. 2015), Subaru/FMOS (Silverman et al. 2015), VLT/VIMOS (VUDS, Le Fèvre et al. 2015; Tasca et al. 2017), Keck/DEIMOS (Hasinger et al. 2018), or the best photometric redshift estimate from Laigle et al. (2016) for galaxies without z_{spec} available.

For the purpose of using this pipeline in future lensed SN searches, the properties of COSMOS sources are compared with expectations for high-redshift SN hosts. Firstly, the cleaned catalog has a redshift distribution peaking at $z \sim 0.8$ with a tail extending to $z \gtrsim 1.5$, akin to the mock lensed SN catalog of Oguri & Marshall (2010), both for LSST-like imaging or for current, shallower surveys probing down to $R \sim 20$–21 (e.g., ZTF, Masci et al. 2019). Secondly, the morphologies and star formation activities can be put in context with properties of SN hosts constrained in the local universe. Using a compilation of >3000 SN and host properties from SDSS-DR8, Hakobyan et al. (2012) show that ~13% of SNe of all types at $z \lesssim 0.1$ explode in galaxies with elliptical or lenticular morphologies, typical of early-type hosts. We augment the quiescent vs. star-forming classes of Laigle et al. (2016) based on redshift-dependent $NUV - r/r - J$ cuts, with Galaxy Zoo morphologies to conclude that our sample is strongly dominated by star-forming galaxies, with ~15%

---

[1] Galaxy Zoo: CANDELS (Simmons et al. 2017) performs similar classifications using deeper, multiband HST images but only over a subset of the COSMOS field (Grogin et al. 2011; Koekemoer et al. 2011) and strongly restricts the sample size.

classified as quiescent. This shows that our sample of sources broadly matches the expected properties of SN hosts.

4.3. Downloading and processing image cutouts

For the lenses, PS1 *gri* image cutouts of $20'' \times 20''$ are downloaded from the PS1 cutout service[2]. We characterized the image depth in individual cutouts with SExtractor (Bertin & Arnouts 1996) and verified that the observing strategy leads to nearly uniform depth. Although it depends on several observing factors, the depth is weakly correlated with the number of individual warp exposures used in a given stack. In particular, it rapidly drops by 0.2–0.3 mag for the 10% of cutouts obtained by coadding less than 8, 10, and 12 frames in *g*, *r*, and *i* bands, respectively. A small fraction of <5% of these PS1 images were discarded from the analysis.

Multiband images of COSMOS galaxies used as lensed sources are taken from the first data release of the HSC SSP (Aihara et al. 2018). The HSC ultra-deep stacks are providing the deepest optical exposures with best image quality over the 2 deg^2 of COSMOS and are well suited for the simulation pipeline. The 5σ point-source sensitivities are 27.8, 27.7, 27.6 mag, in *g*, *r*, *i*, respectively, and seeing conditions are excellent, with median values of $0.92''$, $0.57''$, and $0.63''$ in *g*, *r*, and *i* bands, and negligible variations over the COSMOS field (Tanaka et al. 2017).

We download *gri* cutouts of $10'' \times 10''$, sufficient to enclose all emission from galaxies with $R_{eff} < 1.5''$. Fainter companions within a few arcsec are masked using segmentation maps created in *r* band with SExtractor (using relatively few deblending sub-thresholds, Bertin & Arnouts 1996) to isolate the central galaxy of interest. To overcome the limited spatial resolution of ground-based images, we combine these frames with the HST F814W high-resolution images over the COSMOS field (see Leauthaud et al. 2007; Scoville et al. 2007; Koekemoer et al. 2007) to produce pseudo color images following the steps described in Griffith et al. (2012). First of all, F814W images are aligned and rescaled as if observed in HSC *i* band, and masked HSC frames are resampled with SWarp (Bertin et al. 2002) to the HST scaling of $0.03''$ pix^{-1} using nearest-neighbour interpolation. Secondly, we multiply each resampled frame by an illumination map, defined as F814W divided by HSC *i* band. This process preserves HSC source photometry, and results in *gri* images with high-resolution light profiles and colour gradients with seeing-limited resolution.

4.4. Strong lensing simulations

Due to the limited angular resolution of Pan-STARRS, we focus on the search for wide-separation lens systems with bright arcs that can be easily recognized by eye. We impose a lower limit on the Einstein radius θ_E of mocks of $1.5''$, larger than the median FWHM of PS1 seeing in *gri* bands. This ensures that individual counter-images are well deblended from each other in the mocks (albeit often blended with the lens). Each lens deflector drawn from the LRG catalog is cross-matched with a random COSMOS source at $z_{source} > z_{deflector}$, rejecting pairs with $\theta_E < 1.5''$[3], and repeating the process iteratively to obtain 90 000 lens+source pairs. Focusing on larger Einstein radii amounts to selecting LRGs in the high-mass range, with $v_{disp} \sim 230$–400 km s^{-1}, and redshifts $z_d \sim 0.1$–0.7 representative of the in-

put BOSS sample, and sources in the redshift range $z_s \sim 0.5$–3.0. The pairs mainly cover the θ_E range of 1.5–$3.0''$, which is dominated by galaxy-scale dark-matter lens halos on the high-end of the mass distribution (Oguri 2006), while group-scale lenses contribute predominantly for image separations above $3''$. θ_E values are not uniformly distributed but drop by a factor 100 from $1.5''$to $3.0''$, akin to real galaxy-scale lenses, implying that our CNN will be predominantly exposed to mock systems with $\theta_E \sim 1.5''$.

For each pair, mock images are created with the simulation pipeline described in Schuldt et al. (in prep.). In short, the lens potential is modeled with a Singular Isothermal Ellipsoid (SIE) profile, based on the known v_{disp} and z_d, and using the centroid, axis ratio, and position angle from the *i*-band light distribution, with random perturbations typical of SLACS lenses (Bolton et al. 2008). The combined HSC+F814W cutouts of COSMOS sources are randomly positioned in the source plane, over regions next to the caustics corresponding to magnifications $\mu \geq 5$. The sources are then lensed onto the image plane with the GLEE software (Suyu & Halkola 2010; Suyu et al. 2012). The resulting frames are convolved with the Pan-STARRS PSF model described below, resampled and rescaled using Pan-STARRS zero-points, and eventually coadded with the lens LRG cutouts to obtain the final mock image. The process is repeated for *gri* bands. In order to produce a set of mocks with systematically bright lensing features, we artificially boost the lensed source brightness by one magnitude in all bands. Systems with lensed sources having S/N < 10 in *i* band[4] are placed iteratively closer to the caustics to meet this S/N threshold, or completely discarded.

The Pan-STARRS analysis pipeline computes PSF models at individual positions of stack images over a grid of about $8'$ steps, and interpolates these models to predict the PSF FWHM across the sky (Magnier et al. 2016). This introduces deviations between the modeled and true PSF, since the later varies on very small scales due to stacking of individual exposures with variable FWHM. However, we found that these deviations are usually within 10% when comparing the tabulated FWHMs with those measured on isolated, unsaturated stars from GSC-DR2 (Lasker et al. 2008). We therefore create a library of *gri* PSF models in steps of $0.05''$ FWHM, by stacking PS1 postage stamps of 9 to 11 stars with adequate PSF FWHM. For each mock, lensed arcs are convolved with the PSF model corresponding to the PSF FWHM listed on PS1 tables at the position of the lens LRG.

We generate a total of 90 000 mock lens systems (see Fig. 1). Lens LRGs selected multiple times are rotated by $k\pi/2$ and used only once for a given orientation, with different lensed arc configurations, so the networks never get the exact same image several times as input. The mocks cover realistic source colors and lensing configurations, including quads, near-complete Einstein rings, fold and cusp arcs, and doubles (see Schuldt et al., in prep.). Constraining the source plane positions to large magnifications likely biases our set to lower fractions of doubles than in blind samples of real lenses.

4.5. Photometry of mock lens systems

Focusing the CNN lens search on a subset of the 3 billion sources detected in the PS1 3π survey requires a pre-selection of sources based on their properties released in public catalogs. For this purpose, we compute the photometry of mock lensed systems in the same way as the PS1 image processing pipeline (Magnier

---

[2] http://hla.stsci.edu/fitscutcgi_interface.html
[3] Calculated given the known lens redshift and velocity dispersion and the known source redshift.

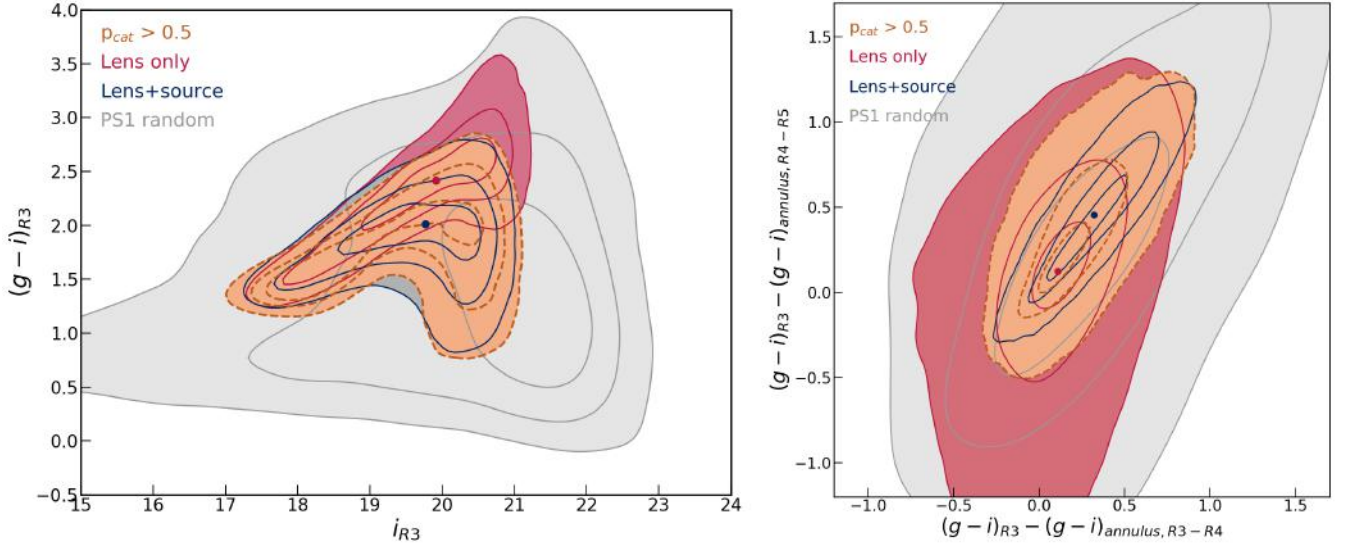[4] Sources fainter than 10 times the local background rms level.

Fig. 2. Aperture magnitudes and colors of galaxies in the lens LRG catalog (red regions) and in the set of 90 000 mock lens systems (blue regions). The red and blue dots show the median of distributions. *Left:* $(g - i)$ vs. i diagram for the R3 aperture, a circular aperture of 1.04″ radius. *Right:* Difference in $(g - i)$ color between the inner R3 aperture and concentric annuli between R3 and R4 (1.76″ outer radius), and between R4 and R5 (3.00″ outer radius). Grey regions mark the position of 100 000 random sources with reliable *gri* aperture photometry selected from the PS1 DR2 catalogs. Orange regions show galaxies with $p_{cat} > 0.5$ on the catalog-level network, which match the colors and magnitudes of mocks lens systems. Solid and dashed lines show the 0.5, 1, and 2σ contours.

et al. 2016). Fixed aperture photometry is particularly important to measure reliable colors. We derive the integrated magnitudes of our mocks within the four smaller PS1 circular apertures of 1.04″(R3), 1.76″(R4), 3.00″(R5), and 4.64″ (R6) radii, which are best suited to capture color gradients due to the presence of lensed arcs at angular separations of 1.5–3.0″ with respect to the lens center. The two largest of these apertures are also expected to be relatively good proxies of the integrated magnitudes of mocks. We use SExtractor in dual-image mode, with a 3σ detection threshold in r-band, and assuming an ideal sky subtraction in PS1 deep stacks (see details in Waters et al. 2016). To compute the aperture magnitudes of a given mock, the image zero-points are taken from the PS1 catalog of stack detections at the position of the LRG used to produce this mock.

The method is tested on LRG-only images by comparing SExtractor estimates with those from the PS1 catalog, for standard stacks. For the four apertures, fitting the distributions of magnitude offsets between these two estimates with Gaussian functions leads to $\mu = 0.00$–0.02 and $\sigma = 0.02$–0.05 in g band, $\mu = 0.00$–0.01 and $\sigma = 0.01$–0.02 in r band, $\mu = 0.00$ and $\sigma = 0.01$–0.02 in i band, which proves the overall robustness of our photometry. Unsurprisingly, the scatter only rises above these average values for the large aperture magnitudes of fainter objects, which mostly enclose background noise. These residual biases up to 0.1–0.2 mag for $\gtrsim 22.0$ mag likely indicate small differences in the local background subtraction between both methods, or the contamination from neighbours which are subtracted by the PS1 pipeline (Magnier et al. 2016) but not with SExtractor. Nonetheless, these offsets remain minor compared to other uncertainties in the analysis. On the contrary, Kron, Petrosian and Sersic photometry are discarded due to systematic biases with respect to values tabulated in PS1 catalogs.

5. Systematic search of strong lenses

The next sections describe the steps followed for the generic lens search on the full Pan-STARRS 3π survey.

5.1. Pre-selecting Pan-STARRS detections

As shown in Fig. 2, the 90 000 mock lens systems have globally bluer colors than the LRG sample due to the relative color of lensed arcs, and they are brighter than ~70% of sources detected in the PS1 stack images. This population of fainter and bluer galaxies can be excluded from the analysis. We use simple color-magnitude cuts in the $(g - i)$ vs. i, $(g - r)$ vs. r, and $(r - i)$ vs. i diagrams for the R3, R4, R5, R6 circular apertures to rule out regions in these diagrams that are not representative of the mocks (i.e. not colored in blue in Fig. 2). These cuts are conservative and include 96% of the mocks, according to the aperture magnitudes obtained in Sect. 4.5, while excluding ~84% of PS1 sources. They are applied to the complete catalog of stack detections from PS1 DR2 using the PanSTARRS1 Catalog Archive Server Jobs System[5], with `detectionFlags3` > 65536 to remove multiple entries and select detections from the optimal stack image (Flewelling et al. 2016).

The stars are removed from the resulting sample using the r-band cuts from Farrow et al. (2014):

$$r_{\mathrm{Kron}} - r_{\mathrm{PSF}} < -0.192 + 0.120 \times (r_{\mathrm{Kron}} - 21) + 0.018 \times (r_{\mathrm{Kron}} - 21)^2.$$

This selection conservatively includes 98% galaxies, those discarded being mainly at the faint end ($r \gtrsim 21$) and with higher magnitudes than our mocks. While these cuts misidentify saturated stars with $r \lesssim 14$ as galaxies (Farrow et al. 2014), such bright sources have already been excluded from the analysis.

Regions with elevated Galactic dust extinction are removed as strong reddening could alter our selection on the catalog level. The interstellar dust reddening 2D map of Schlegel et al. (1998) are loaded with the `dustmaps` python interface from M. Green (2018). After converting to PS1 bandpasses using coefficients in Table 6 of Schlafly & Finkbeiner (2011), we apply a reddening threshold of E$(g - i) < 0.3$. These steps result in a catalog of 23.1 million galaxies for classification.

---

[5] http://casjobs.sdss.org/CasJobs

5.2. Applying machine learning to the Pan-STARRS photometry

Limitations due to download speed of PS1 cutouts from the archive can be overcome by further reducing the size of this catalog with additional selection criteria. The simple color/magnitude cuts applied to the complete PS1 catalog do not capture all photometric properties of mock lens systems, such as their precise locus on two-dimensional color/color and color/magnitude diagrams or their radial color gradients. For instance, Figure 2 indicates that mocks are generally redder within the smaller R3 aperture of 1.04″ radius than within external, concentric annuli between R3 and R4, and between R4 and R5. These gradients are caused by the presence of bluer, lensed arcs at >1.5″ from the lens center and disappear on the LRG-only sample. To exploit this information, we train a simple fully-connected neural network on the photometry of mocks and random PS1 sources using aperture fluxes that ensure robust colors.

The data set contains *gri* fluxes in the four apertures for 90 000 lens and 90 000 non-lens examples as inputs, and the ground truth labels of 1.0 and 0.0, respectively, as outputs for binary classification. The negative examples are fluxes of random sources that match our loose color/magnitude *gri* cuts in Sect. 5.1. The data set is split into training, validation, and test sets with respective fractions of 56%, 14%, and 30%. All fluxes are normalized to the average over the entire data set in order to speed up the learning process. The network architecture consists of 12 dimensional input data, three fully connected hidden layers of 50, 30, and 5 neurons each, with Rectified Linear Unit (ReLU, Nair & Hinton 2010) non-linear activations[6], and a single-neuron output layer with sigmoid activation[7].

During the training phase, the network derives a model for classifying galaxies in the training set as lenses or non-lenses according to their input photometry, as briefly summarized with the following stages. After the weight parameters and bias in each neuron are initialized, a subset of the training data is passed through the entire network to calculate predicted labels (forward propagation), and the difference between predictions and ground truth labels is quantified with a loss function L. This information is propagated to the network weights and biases (back propagation, Rumelhart et al. 1986) which are then modified using a gradient descent algorithm to minimize the total loss and improve the model. These stages are repeated iteratively to perform a complete pass through the entire training set, corresponding to one epoch, and then over multiple epochs until the model reaches optimal accuracy. After each epoch, the validation loss is evaluated by classifying inputs from the validation set, in order to determine whether the decrease in training loss reveals better performance or an overfitting to the training set. After training, the network performance is finally quantified using independent data from the test set. Further details can be found in the review of LeCun et al. (2015).

Network parameter optimization is performed via mini-batch stochastic gradient descent, a common variant that consists of splitting the training set into small batches and adjusting the weights according to the average corrections over each batch. Our network minimizes the cross-entropy loss function which
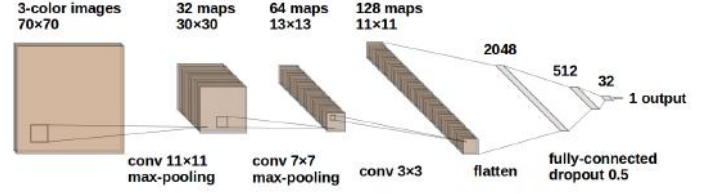

Fig. 3. Architecture of the convolutional neural network, inspired from LeNet (LeCun et al. 1998), and comprised of three convolutional layers with 11×11, 7×7, and 3×3 kernel sizes, and 32, 64, and 128 filters, respectively, followed by three fully connected hidden layers with 2048, 512, and 32 neurons. ReLU activations are applied between each layers. Max-pooling layers with 2×2 kernel sizes and stride = 2 are inserted after the first two convolutional layers, and dropout of 0.5 is used before the fully connected layers.

penalizes robust and incorrect predictions, and is expressed as follows for a binary classification problem

$$L(y, p) = -\frac{1}{N} \sum_{i=0}^{N} y_i \log(p_i) + (1 - y_i) \log(1 - p_i) \qquad (1)$$

where y_i are the ground truth labels, and p_i the network predictions, namely scores in the range [0,1] resulting from the sigmoid activation on the output layer. The loss is computed over each batch of size N. To avoid unbalanced splits of the data set, we use 5-fold cross-validation that consists of reshuffling the training and validation sets and building the performance metrics. Cross-validation runs trained over 500 epochs are used to optimize the neural network hyperparameters with a grid search, varying the learning rate over the range [0.0001, 0.1] and the weight decay over [0.00001, 0.01], with momentum fixed to 0.9. We train a final network with the entire data set using an optimal learning rate and weight decay of 0.001 and 0.00001, respectively, and applying early stopping at epoch 193 that matches the lowest average loss over the cross-validation runs.

Among the 23.1 million input galaxies, 1 050 207 are assigned scores $p_{cat} > 0.5$ indicating that their *gri* aperture photometry is consistent with the mocks. Fig. 2 illustrates the network predictions by comparing the colors and magnitudes of random galaxies, mocks, and galaxies having $p_{cat} > 0.5$. The good agreement between 2σ contours of mocks and $p_{cat} > 0.5$ shows that the network correctly captures the position of mocks in color/magnitude diagrams, as well as their color variations within different apertures. Moreover, our photometric selection is successfully tested on the aperture fluxes of known strong lensing systems listed as grade A or B with $\theta_E = 1.0$–3.0″ in the MasterLens database[8], and with lensed arcs visible in the PS1 stack images. We therefore keep these 1 050 207 galaxies for CNN classification.

5.3. Training the convolutional neural networks

Data sets for the CNNs include 180 000 images in *g*, *r*, and *i* bands with the same fraction of positive (lens) and negative (non-lens) examples. Positive examples are taken from the sample of simulated lens galaxies with $\theta_E > 1.5$″ described in Sect. 4.4. The choice of negative examples is strongly influencing the network predictions and is modified iteratively to improve the network performances (see Sect. 5.5). In short, we boost the fraction of galaxies with specific morphological types using incorrect identifications of strong lenses in previous networks. This

---

[6] ReLU(x) = max(x,0)

[7] sigmoid$(x) = \frac{1}{(1+e^{-x})}$
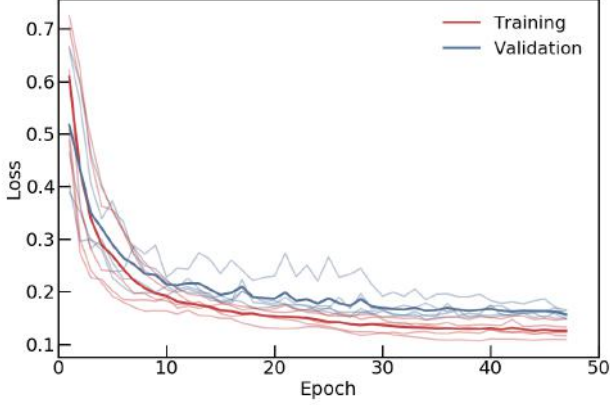
[8] http://admin.masterlens.org

Fig. 4. Training of the CNN with optimized hyperparameters and using early stopping. The training loss (red curve) and validation loss (blue curve) are taken as the average of all cross-validation runs (light red and blue curves).
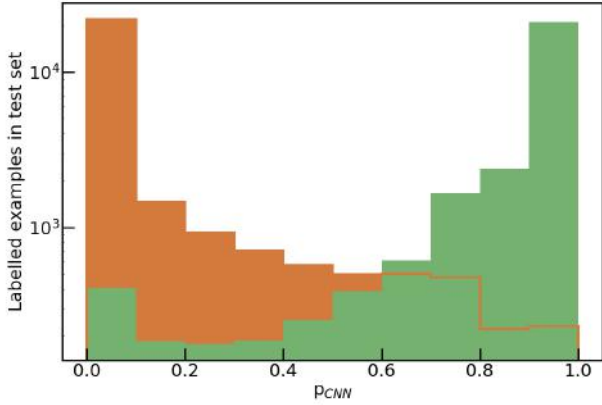

Fig. 5. Distribution of network predictions compared with the ground-truth for lenses (green) and non-lenses (orange) in the test set.

allows the network to learn how to discriminate strongly lensed arcs from the usual contaminants such as extended arms of low redshift spirals, lenticular galaxies, and mergers, and to distinguish isolated LRGs from LRGs with the relevant strong lensing features depicted in the mocks. Our resulting set of 90 000 negative examples includes:

- 30% LRGs selected directly from the catalog of SDSS LRGs on the high-end of the mass distribution used to create the mocks,
- 20% spirals classified as likely face-on galaxies in Galaxy Zoo 2 (Willett et al. 2013) and with r-band Sersic radii $<4.5''$ from PS1 (Flewelling et al. 2016), to restrict to blue spiral arms with similar extension as the lensing features present in the mocks,
- 10% smooth, isolated galaxies from Galaxy Zoo 2 without bright companion and bluer colors than LRGs,
- <1% galaxies with apparent dust lanes identified in Galaxy Zoo 2 (Willett et al. 2013),
- 32% randomly selected galaxies from the PS1 catalog, including diverse types, groups and mergers, and with negligible contamination from the rare strong lenses,

- 7% false positives from previous neural networks selected by visually classifying candidates with scores > 0.9.

Negative examples are not included in the $p_{\text{cat}} > 0.5$ sample to be classified with the CNN, but they broadly follow the same color and magnitude distributions in gri bands. Some examples are shown in Fig. 1. The data set is split into training, validation, and test sets with the same proportions as before (Sect. 5.2).

We use data augmentation and apply random shifts between –5 and +5 pixels to all images so the network becomes invariant on small positional offsets. This results in input images of 70×70 pixels which conservatively include all emission from the central galaxy of interest. All survey galaxies in the set of negative examples are unique, and LRGs used multiple times in the sample of mocks have been rotated by $k\pi/2$ so they appear only once with a given orientation in the set of positive examples. This ensures that the network is not sensitive to preferential orientations. Other common image augmentation techniques, such as image stretching, normalisation and rescaling (e.g., Petrillo et al. 2017, 2019) have been discarded as they do not significantly improve the learning process.

The CNN architecture is inspired from LeNet (LeCun et al. 1998) and from the lens modeling CNN of Schuldt et al. (in prep.). After the $70 \times 70 \times 3$ input layer, it contains three convolutional layers with 11×11, 7×7, and 3×3 kernel sizes, and 32, 64, and 128 filters, respectively, followed by three fully connected hidden layers with 2048, 512, and 32 neurons (see Fig. 3). ReLU activations act as non-linear transformations between each one of these layers. Max-pooling layers (Ranzato et al. 2007) with 2×2 kernel sizes and stride = 2 are inserted after the first two convolutional layers and are essential to make the CNN invariant to local translations of the relevant features in gri image cutouts, while reducing the network parameters. Dropout regularization (Srivastava et al. 2014) with a dropout rate of 0.5 is applied before the fully connected layers. This is an efficient regularization method that consists of randomly ignoring neurons during training in order to reduce overfitting on the training set and improve the CNN generalization. The output layer consists of a single neuron with sigmoid activation and results in a score, p_{CNN}, in range [0, 1] which corresponds to the network lens/non-lens prediction[9]. Our CNN with moderate depth is well suited for binary classification of small PS1 cutouts.

During the training process, the CNN learns the relevant patterns in gri images by adjusting the convolutional kernel weights, through a minimization of the binary cross-entropy loss between ground truth and predicted labels. After the gradient calculation and optimization, information learned by the network is stored in the two-dimensional filters. As for the catalog-level network, we use mini-batch gradient descent with a batch size of 128 and performed five cross-validation runs. We find an optimal learning rate and weight decay of 0.0006 and 0.001, respectively, using a grid search with momentum fixed to 0.9. The number of training epochs is then chosen from the minimum average validation loss over the cross-validation runs, which corresponds to optimal network performance without overfitting.

The evolution of the training and validation loss for the network with optimized hyperparameters is shown in Fig. 4, until epoch 47 which corresponds to the lowest validation loss. The gap between both curves (generalization gap) is small, showing that the model predictions do not deteriorate much on new data with similar properties as the training set. The final network performances are characterized with the test set which was not

---

[9] For uncalibrated networks, this score differs from the likelihood of correct classification.
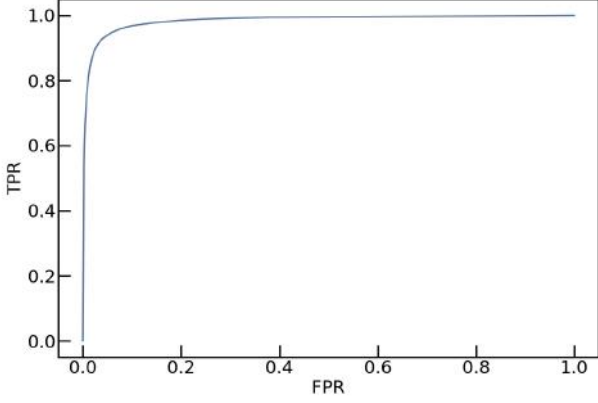
Fig. 6. Receiver Operating Characteristic curve for the trained CNN showing the true position rate (TPR) as function of the false positive rate (FPR) for different lens identification thresholds. The corresponding area under curve (AUC) is 0.985.

seen during training and validation and contains about 54 000 entries. In Fig. 5, we show the model probability predictions for all lens and non-lens examples in the test set. Lenses dominate the distribution for $p_{CNN} > 0.6$. The model reaches 94.2% accuracy, 93.1% purity and 95.5% completeness on this set suggesting good pattern recognition abilities on new images[10]. In addition, the Receiver Operating Characteristic (ROC) curve in Fig. 6 illustrates the relation between the true positive rate (TPR, the number of lenses correctly identified over the total number of lenses) and the false positive rate (FPR, the number of non-lenses identified as lenses over the total number of non-lenses) in our trained model. The curve is obtained by varying the network probability threshold for lens identification in the range [0, 1], and an ideal network would correspond to an area under curve (AUC) of 1. Our CNN gives AUC = 0.985, and can correctly identify 95.5% of lenses in the test set with a FPR of 7.1% using $p_{CNN} > 0.5$, or 77.0% of lenses in the test set with a FPR of 0.8% using $p_{CNN} > 0.9$.

After optimizing hyperparameters and quantifying the performance of the network on the test set, we train a final CNN with the complete data set of 180 000 labelled images and we fix the resulting model parameters to classify the 1 050 207 galaxies with $p_{cat} > 0.5$.

5.4. Evaluating the network performance

The performance of the network is further evaluated on galaxies with various properties on the test set. Fig. 7 depicts the normalized distributions of scores for positive examples in different bins of θ_E, θ_E/R_{eff}, and r_{Kron}, where R_{eff} is the effective radius from the r-band Sersic fit of the LRG-only image (Flewelling et al. 2016). Somewhat counterintuitively, scores are closer to 1.0 for lenses with $\theta_E < 2''$. The low fraction of $\theta_E > 2''$ in the training set might explain the slightly lower CNN performance on these systems, which generally do not have the most challenging morphologies. Histograms for θ_E/R_{eff} demonstrate the ability of the network to assign p_{CNN} closer to 1.0 for mocks

with Einstein radius larger than the effective radius of the lens light distribution, where lensed arcs are in principle better deblended from the lens. We also find a higher fraction of scores $p_{CNN} > 0.9$ for lens LRGs with higher r_{Kron} (i.e. fainter LRGs), perhaps because the brightest lenses outshine the lensed source emission. Nonetheless, these variations remain generally minor.

Finding acceptable network performances on the test set might be misleading as it relies on our choices in simulating the strong lenses and assembling a set of negative examples. A valuable independent test consists of applying the CNN to strong lenses from the literature. For that purpose, we collect all grade A and B galaxy-scale lenses in the MasterLens catalog, restricting to Einstein radii ~1–3″ similar to the range probed by our 90 000 mocks. These systems were discovered from various techniques including the identification of emission lines from star-forming galaxies behind LRGs using spatially-integrated spectra (SLACS, Bolton et al. 2008), and the analysis of high-quality imaging from HST (e.g., in COSMOS, Faure et al. 2008) or deep multiband surveys (e.g., CFHTLS SL2S, Cabanac et al. 2007; Gavazzi et al. 2014; More et al. 2016). Most of these lenses are not detectable in *gri* Pan-STARRS stacks and need to be excluded from our test set. We thoroughly scanned all PS1 *gri* single-band and 3-color images of this sample to find those with detected lensed arcs, and assembled a test set of 16 systems. While these published lenses have colors, z_d, z_s, and configurations similar to our mocks, some of their multiple images are strongly blended with the lenses and difficult to identify with PS1 data.

Pan-STARRS cutouts of these 16 lenses are scored with our trained neural network and the results are presented in Fig. 8. A total of 14/16 lenses are correctly identified as $p_{CNN} > 0.5$ by the CNN, while 9/16 and 7/16 have higher scores $p_{CNN} > 0.8$ and $p_{CNN} > 0.9$, respectively. SL2SJ0217−0513 and SDSSJ1112+0826 are the two incorrect classifications. SL2SJ0217−0513 has a faint lens galaxy falling in the upper range of the redshift distribution ($z_d = 0.646$) and blended with a faint blue arclet. It is worth noting that the network performs better for SDSSJ1110+3649 ($p_{CNN} = 0.971$) which has a similar morphology to SL2SJ0217−0513, but with the addition of a low S/N, blue counter image on the other side of the lens galaxy. SDSSJ1112+0826 has typical properties of our mocks but lacks a bright counter image. On the other hand, lenses with well-detected and deblended arcs and counter images (e.g., SDSSJ1430+4105, SDSSJ0201+3228, CSWA21) have high scores, showing that the network is able to extract relevant features.

Our comparison extends to systems with Einstein radii below the 1.5″ cutoff applied to our simulations. The CNN performance in this regime remains acceptable, as illustrated by the scores of 0.786, 0.612, and 0.971 assigned respectively to SDSSJ1134+6027, SDSSJ2156+1204, SDSSJ2231−0849 that have $\theta_E \sim 1.1''$. In contrast, with $\theta_E = 3.26''$ due to its group-scale environment (Auger et al. 2013), CSWA21 falls on the upper range of the Einstein radius distribution that is underrepresented with only a few hundred examples in our training set. This system is nonetheless given a score of 0.873 and confirms that the CNN can identify these simple configurations. Interestingly, the four systems with ≥ 4 magnified images according to the MasterLens database have $p_{CNN} > 0.9$. The small number of test lenses however prevents robust estimates of the method purity and completeness.

---

[10] Accuracy is defined as the sum of true positives and true negatives over the total number of systems (lenses + non-lenses), and purity is defined as the number of lenses correctly identified with $p_{CNN} > 0.5$ over the number of systems with $p_{CNN} > 0.5$.
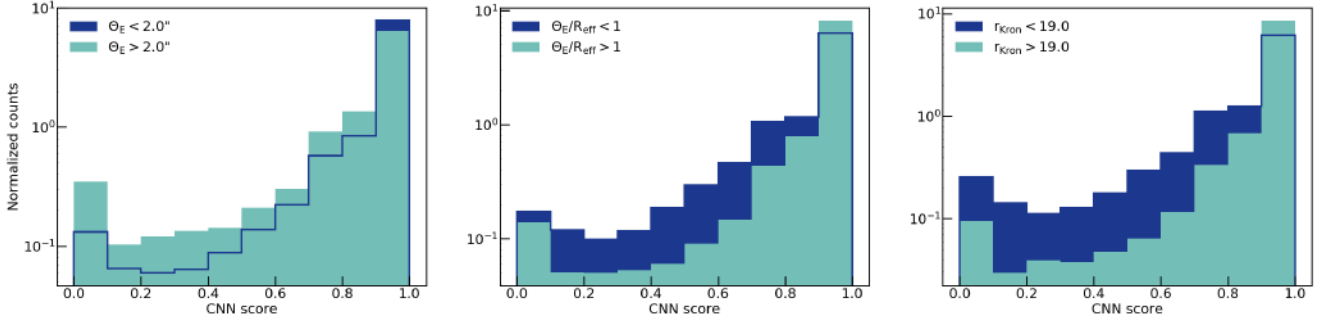
Fig. 7. Normalized distributions of CNN scores for mocks lenses included as positive examples in the test set, for different ranges of Einstein radii (left), θ_E/R_{eff} (middle), and r_{Kron} (right).

Fig. 8. Three-color images of the 16 confirmed lens systems in the MasterLens database that have clear strong lensing signatures in Pan-STARRS images, and Einstein radii of 1–3″ similar to our mocks. The CNN scores are displayed at the top of each panel. Images are $15'' \times 15''$.

5.5. Discussion on the CNN training

The final version of the CNN from Sect. 5.3 is selected from a range of networks with different architectures, after testing the impact of the training set content. To identify the optimal network, we compare scores assigned to the 16 known test lenses and require low false positive rates by examining *gri* cutouts of the few hundred galaxies with highest scores p_{CNN}. Overall, different choices of positive and negative examples have much stronger impact than changes in the CNN architecture.

The sets of negative examples tested include: (1) random PS1 sources drawn from the pre-selection in Sect. 5.1; (2) typical LRGs selected as in Eisenstein et al. (2001), mostly less massive than LRGs in mocks; (3) high-mass LRGs similar to those used in Sect. 4; (4) a combination of LRGs, face-on spirals, and random sources (varying the fractions of LRGs and contaminants). Scores on the MasterLens systems from CNNs using sets (1) and (4) are comparable to those in Fig. 8, but introduce an overwhelming number of $\gtrsim 400\,000$ galaxies with $p_{CNN} > 0.5$ and $\gtrsim 250\,000$ with $p_{CNN} > 0.9$ implying high false positive rates,

and are ruled out. Other sets of positive examples are tested by (1) modifying the θ_E lower limit, and (2) suppressing the artificial boost in arc brightness to get more realistic lens/source flux ratios. Both CNNs trained on fainter arcs, more strongly blended with the lens significantly reduce the fraction of genuine lens examples with scores $p_{CNN} \sim 1$ and are also discarded.

Our tests on the architecture include: (1) adding and removing one convolutional layer, or one fully-connected layer; (2) changing the number of neurons, the kernel sizes or number of feature maps in these layers; (3) using smaller or larger strides on the max-pooling layers; (4) modifying the dropout rates; (5) implementing batch normalization (Ioffe & Szegedy 2015). Each of these changes degrade the network performance as measured from the loss and ROC curves on the test set, and from the 16 MasterLens systems. Using dropout normalization before fully connected layers (as in Fig. 3) turns out to be the most efficient solution to reduce overfitting.

5.6. Visual classification

Galaxies with high CNN scores, p_{CNN}, are visually inspected by different authors to assign a final grade. We started classifying galaxies with p_{CNN} close to 1.0, and progressively lowered the threshold to introduce additional galaxies until the fraction of reliable candidates from visual inspection became too low.

We grade the single-band and 3-color PS1 cutouts in *gri* bands, zoomed to $12'' \times 12''$, and optimally displayed with linear and arcsinh scaling using dedicated scripts to emphasize faint, sometimes blended strong lensing features[11]. To aid the visual classification, we plot *grz* single-band and 3-color postage stamps from the DESI Legacy Imaging Surveys that significantly overlaps the PS1 3π survey footprint on the extragalactic Northern sky, and that provides slightly deeper, higher quality images (Dey et al. 2019), and we plot residual frames from subtraction of the best-fit light profile. On smaller regions of the sky, we also include *gri* images from HSC DR2 wide-field surveys (Aihara et al. 2019). The set of CNN candidates is divided into four equal parts, each inspected either by R. C., S. S., S. H. S., or S. T., in order to assign one of the following *grades*: 0: non-lens, 1: maybe a lens, 2: probable lens, 3: definite lens, similarly to Sonnenfeld et al. (2018) and Jacobs et al. (2019a). All candidates with grades ≥ 2 from this first iteration are then inspected by the three other authors, so final grades were averaged over the four authors. The output list of candidates corresponds to average grades ≥ 2.

---

[11] code adapted from https://github.com/esavary/Visualisation-tool

Fig. 9. *Top:* Pan-STARRS 3-color *gri* images of a subset of candidates with grades ≥ 2 from visual inspection of CNN scores $p_{CNN} > 0.9$ (the complete figure is available in Appendix A). Numbers displayed on top of each panel are CNN scores (p_{CNN}, left) and average visual grades (right). Candidates with PS1 names marked in orange have been previously published in the literature (see Table 1 and Sect. 6.1) Those marked in blue show unambiguous spectral signatures of high-redshift background sources in our inspection of SDSS BOSS DR16 data. *Bottom:* Examples of random false positives with $p_{CNN} = 1$. All cutouts are $15'' \times 15''$.

Non-lenses are galaxies clearly identified as nearby spirals, ring galaxies, groups, or other contaminants from their morphology, or cutouts with artifacts. Candidates listed as grade 1 have faint companions and/or weakly distorted features suggesting possible strong lensing signatures, but may also correspond to galaxy satellites or spiral arms. Probable lenses show multiple elongated sources with similar colors, and orientation and angular separation expected for counter-images, while the available 3-color images cannot firmly rule out contaminants. Those assigned grades of 3 have similar, although brighter, non-blended and unambiguous signatures of galaxy-scale strong lenses.

6. Results and discussion

6.1. Final candidates from visual inspection

Out of the 1.1 million galaxies the CNN scores 598 130 with $p_{CNN} = 0$, and 105 760, 12 382, and 1714 as candidate lenses with $p_{CNN} > 0.5$, $p_{CNN} > 0.9$, and $p_{CNN} = 1$, respectively. Scores $p_{CNN} > 0.5$ amount to 10% of sources ranked by the CNN, and only 0.5% of the input catalog of 23.1 million galaxies. The human inspection process is necessary to increase purity of the candidate sample. However, a systematic visual classification of galaxies with $p_{CNN} > 0.5$ would be unrealistic and we use a higher p_{CNN} threshold which impacts the purity and completeness in a way that is difficult to quantify. Predictions for mock lenses on the test set (see Fig. 5) and for known lenses (see Fig. 8) suggest that the majority of good candidates have scores

Name	RA	Dec	p_{CNN}	Grade	g_{Kron}	r_{Kron}	i_{Kron}	g_{aper}	r_{aper}	i_{aper}	Redshift	Notes
PS1J2226+0041	22:26:09	+00:41:42	0.990	3.00	...	20.59	19.37	23.34	21.9	20.63	0.6471[*]	(a), (b), (c)
PS1J1821+7130	18:21:40	+71:30:10	1.000	3.00	18.66	17.61	17.19	20.12	19.04	18.62	...	
PS1J1647+1117	16:47:04	+11:17:49	0.951	3.00	19.47	18.56	18.00	20.98	19.92	19.32	...	
PS1J1559+3147	15:59:23	+31:47:12	1.000	3.00	18.19	17.18	16.58	19.77	18.74	18.15	0.1489[*]	
PS1J1508−1652	15:08:10	−16:52:38	1.000	3.00	...	18.95	18.39	22.42	20.65	19.88	...	
PS1J1421−0536	14:21:28	−05:36:51	1.000	3.00	19.57	18.59	17.97	21.22	19.99	19.29	...	
PS1J1415+1112	14:15:31	+11:12:08	0.993	3.00	19.54	18.30	17.65	21.05	19.81	19.16	0.3155[*]	
PS1J1322−0501	13:22:27	−05:01:34	0.995	3.00	...	20.18	19.33	23.26	21.55	20.66	...	
PS1J1113+0104	11:13:57	+01:04:05	0.951	3.00	...	20.77	19.49	23.21	21.81	20.70	0.6402[*]	
PS1J0919+0336	09:19:05	+03:36:39	0.919	3.00	20.28	19.12	18.41	22.12	20.68	19.90	0.4440[*]	(c), (l)
PS1J0353−1706	03:53:46	−17:06:39	0.933	3.00	...	20.35	19.50	23.47	21.72	20.63	...	(a)
PS1J0324−1020	03:24:49	−10:20:53	0.999	3.00	20.72	19.83	18.93	22.48	21.20	20.22	...	
PS1J0211−1938	02:11:01	−19:38:10	0.944	3.00	20.42	19.29	18.80	22.05	20.66	19.97	...	
PS1J0141−1713	01:41:06	−17:13:24	1.000	3.00	...	20.08	19.19	23.30	21.54	20.62	0.56	(a), (d)
PS1J2348+0148	23:48:45	+01:48:35	0.989	2.75	22.00	20.72	19.32	23.12	21.64	20.43	0.5902[*]	
PS1J2336−0207	23:36:10	−02:07:35	1.000	2.75	20.43	19.52	18.91	21.92	20.80	20.06	0.4942[*]	
PS1J2248−0103	22:48:01	−01:03:00	1.000	2.75	19.44	18.15	17.56	20.92	19.62	18.95	0.2772[*]	(e)
PS1J2247+1801	22:47:20	+18:01:21	1.000	2.75	19.97	18.53	17.96	21.59	20.16	19.57	0.3427[*]	
PS1J2233+3012	22:33:34	+30:12:23	0.998	2.75	19.93	18.31	17.68	21.64	20.06	19.41	0.3605[*]	
PS1J2202+0614	22:02:52	+06:14:50	1.000	2.75	18.52	17.40	16.83	19.87	18.78	18.22	0.17	
PS1J2200−1024	22:00:47	−10:24:27	0.997	2.75	20.82	19.07	18.34	22.02	20.15	19.45	...	
PS1J1926−2138	19:26:18	−21:38:20	1.000	2.75	16.48	15.90	15.65	17.80	16.98	16.69	...	
PS1J1749+2330	17:49:12	+23:30:36	0.992	2.75	...	18.65	17.86	22.06	20.37	19.76	...	
PS1J1655+0406	16:55:09	+04:06:13	1.000	2.75	18.30	17.77	17.32	20.03	19.33	18.86	...	
PS1J1644+1121	16:44:08	+11:21:30	0.998	2.75	17.85	17.28	16.87	20.03	19.17	18.60	0.14	
PS1J1555+4151	15:55:18	+41:51:39	1.000	2.75	20.96	19.93	19.02	22.25	21.32	20.35	0.5553[*]	(c)
PS1J1553−0142	15:53:38	−01:42:34	0.995	2.75	21.26	19.87	18.80	22.90	21.30	20.32	0.40	
PS1J1445+3649	14:45:54	+36:49:49	0.960	2.75	19.85	18.33	17.66	21.06	19.52	18.89	0.3551[*]	
PS1J1439+0721	14:39:37	+07:21:01	0.913	2.75	20.80	19.48	18.65	22.25	20.63	19.79	0.4795[*]	
PS1J1422+4246	14:22:41	+42:46:08	0.983	2.75	21.43	20.46	19.63	22.89	21.86	20.82	0.6047[*]	(e)
PS1J1411+2313	14:11:05	+23:13:57	0.955	2.75	19.80	18.19	17.58	21.29	19.74	18.93	0.3508[*]	
PS1J1349+0537	13:49:15	+05:37:51	0.995	2.75	20.78	19.57	18.64	22.33	20.75	19.80	0.5055[*]	
PS1J1241+2721	12:41:37	+27:21:25	1.000	2.75	20.70	20.15	19.64	22.10	21.40	20.59	0.50	
PS1J1206+2336	12:06:51	+23:36:02	1.000	2.75	19.95	18.92	18.46	21.57	20.11	19.62	0.25	
PS1J1111+4329	11:11:55	+43:29:11	1.000	2.75	...	20.01	19.31	23.21	21.75	20.57	0.6370[*]	
PS1J0921+0214	09:21:37	+02:14:09	0.979	2.75	19.57	18.21	17.71	21.41	20.09	19.42	0.3191[*]	(f), (l)
PS1J0907+4233	09:07:28	+42:33:02	1.000	2.75	19.67	18.75	18.05	21.32	20.40	19.51	0.4950[*]	
PS1J0737+1914	07:37:10	+19:14:36	0.989	2.75	20.03	18.90	18.31	21.69	20.25	19.54	0.3528[*]	
PS1J0717+4624	07:17:41	+46:24:31	1.000	2.75	19.61	18.02	...	21.18	19.65	19.12	...	
PS1J0520−2008	05:20:03	−20:08:04	0.929	2.75	19.19	18.78	18.44	20.57	20.13	19.85	...	

Table 1. Final list of galaxy-scale strong lens candidates with lens LRGs from our systematic search in Pan-STARRS (the complete table is available in Appendix A). These systems are selected as high confidence candidates with CNN scores > 0.9, and average grades ≥ 2.0 from visual inspection. Columns are: source name; right ascension; declination; output score from the CNN; average of the visual grades from four authors; g-, r-, and i-band Kron magnitudes of the lens and source blends from the PS1 catalog; g-, r-, and i-band aperture magnitudes of 1.04″ radii covering the lens central regions; SDSS photometric redshifts or spectroscopic redshifts marked as [*] where available; previously published confirmed or candidate systems (grades A and B or equivalent). References are the following: (a) Jacobs et al. (2019a), (b) Diehl et al. (2017), (c) Sonnenfeld et al. (2018), (d) Huang et al. (2019), (e) Wong et al. (2018), (f) Petrillo et al. (2019), (g) Stark et al. (2013), (h) Auger et al. (2009), (i) Jacobs et al. (2019b), (j) Lemon et al. (2019), (k) Wang et al. (2017), (l) Jaelani et al. (2020), and (m) Schirmer et al. (2010).

p_{CNN} > 0.9 with only a few more in the range $0.5 < p_{CNN} < 0.9$, and we therefore started inspecting all 12 382 with $p_{CNN} > 0.9$. As the fraction of visual grades ≥ 2 quickly drops with decreasing CNN scores, down to ≲ 1% when extending to $0.8 < p_{CNN} < 0.9$, we restricted our final classification to $p_{CNN} > 0.9$.

Our selection results in 321 high-confidence candidates with grades ≥ 2 (hereafter, grades refer to the average grades from the visual inspectors). Respective fractions of 36%, 34%, and 30% of these candidates have scores in the intervals $0.99 < p_{CNN} \leq 1.00$, $0.95 < p_{CNN} \leq 0.99$ and $0.90 < p_{CNN} \leq 0.95$, which demonstrates that the CNN learns meaningful information and assigns high scores for most of the probable or definite lenses. The rate

of grades ≥ 2 over the 12 382 galaxies with $p_{CNN} > 0.9$ is about 2.5%. This fraction is slightly lower but comparable to previous CNN lens searches using deeper, higher quality imaging surveys (KiDS DR4, DES Year 3, Petrillo et al. 2019; Jacobs et al. 2019a). This is not surprising as some of these searches have focused on catalogs of LRGs with robust photometry and are less subject to contamination by low-redshift spirals. Obtaining equivalent performance suggests that our initial catalog-level classification plays an important role in our systematic search that balances the suboptimal imaging quality of the PS1 3π survey. Finally, 37 additional candidates from previous CNNs with $p_{CNN} = 1.0$ and grades ≥ 2 are included (see Sect. 5.5), bring-
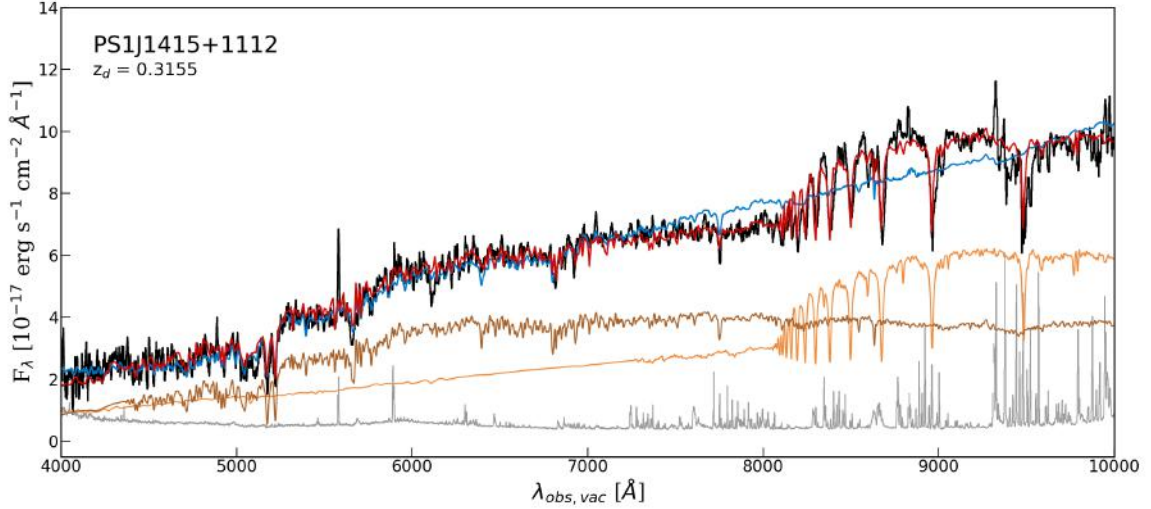
Fig. 10. Pan-STARRS lens candidate with prominent Balmer absorption features from a background galaxy at $z_s = 1.185$ blended with the BOSS spectrum of the lens LRG at $z_d = 0.3155$. The black and grey lines show the spectrum observed with a fiber of $2''$ diameter and the 1σ noise level, respectively, and the blue line corresponds to the best-fit LRG template from the automated SDSS pipeline at $\lambda < 8000$ Å (see inset), which poorly fits the continuum and Balmer lines at longer wavelengths. The red line shows that combining the SED templates of an LRG at $z_d = 0.3155$ (brown curve) and a recently quenched galaxy at $z_s = 1.185$ (orange curve) correctly fits the spectrum over the entire range (see details in text).

ing the total number of resulting lens candidates to 358 from our two-step search.

Examples of good candidates and false positives (grades ≤ 1) after visual inspection are shown in Fig. 9. In most cases, false positives belong to specific galaxy types frequently misclassified by the network such as nearly face-on spirals with obvious and extended arms, nearby lenticular galaxies, and bright LRGs with faint unlensed companions. Galaxy groups, mergers with perturbed morphologies, and cutouts with background artifacts are more rare. Other ambiguous systems listed as false positives are galaxies with red bulges and faint arms, with color gradients or companions, where all components are blended and mimic lensed arcs.

The PS1 lens candidates are cross-matched with galaxy-scale strong lenses from previous searches with the status of spectroscopally confirmed or candidate systems, by building upon and expanding the current MasterLens database. We compiled grade A and B systems (or equivalent) from a number of recent searches based on optical/near-infrared imaging from DES (Diehl et al. 2017; Jacobs et al. 2019b,a), CFHTLS (More et al. 2016; Jacobs et al. 2017), KiDS (Petrillo et al. 2017, 2019; Li et al. 2020), DESI (Huang et al. 2019), and HSC (Wong et al. 2018; Sonnenfeld et al. 2018; Jaelani et al. 2020; Sonnenfeld et al. 2020). Since our network may also be sensitive to lensed quasars with colors and configurations similar to our mock lenses, we also cross-matched with the all-sky database of ~220 confirmed lensed quasars in the literature (Lemon et al. 2019, and references therein)[12], and with previously identified lensed quasars from HSC (Chan et al. 2019) and from PS1 (Rusu et al. 2019). For the candidates not included in those tables, we searched in the SIMBAD Astronomical Database[13].

To our knowledge, besides the test lenses from the MasterLens database, 23 of our 358 CNN candidates are already listed in the literature and corresponding references are listed in Table 1. The vast majority of them are also galaxy-scale strong lens candidates from ground-based multi-

band imaging searches and lack both spectroscopic and high-resolution imaging follow-up. The only galaxy-galaxy lens systems confirmed with spectroscopy and/or space-based imaging are PS1J0143+1607, PS1J0145−0455, PS1J2343−0030, and PS1J0454−0308. Firstly, PS1J0143+1607 is CSWA 116, discovered through the search of blue lensed features near LRGs in SDSS imaging (Stark et al. 2013). Its properties ($z_d = 0.415$, $z_s = 1.499$, $\theta_E = 2.7''$) are very similar to our mock lenses, and the system was assigned $p_{CNN} = 1.0$ and a visual grade of 2.75. Secondly, PS1J0145−0455 is CSWA 103, also presented by Stark et al. (2013), and has $z_d = 0.633$, $z_s = 1.958$, and $\theta_E = 1.9''$, akin to our mocks. It has $p_{CNN} = 1.0$ and a visual grade of 2.50. Thirdly, PS1J2343−0030 is a SLACS lens with $z_d = 0.181$ and $z_s = 0.463$ which was discovered and modeled by Auger et al. (2009) using SDSS spectroscopy and HST imaging. It has an Einstein radius of $1.5''$, higher than the majority of lenses in the SLACS sample, which explains its elevated scores from the CNN ($p_{CNN} = 0.917$) and PS1 cutout inspection (2.50). Lastly, PS1J0454−0308 ($p_{CNN} = 1.000$ and grade = 2.75) is a peculiar system thoroughly studied in Schirmer et al. (2010), where the main lens is the brightest elliptical galaxy of a fossil group at $z = 0.26$ only $8'$ from the MS0451−0305 cluster at $z = 0.54$. The HST F814W frame clearly resolves the background source into an extended arc and a compact counter image, corresponding to $\theta_E = 2.4''$. Most other galaxy-galaxy lenses in the literature were missed by our selection due to limited PS1 depth or lens configurations not represented in our mocks (e.g., higher Einstein radii). Finally, two of these 23 published systems are confirmed lensed quasars. PS1J2350+3654 ($p_{CNN} = 1.0$ and grade of 2.25) was discovered in Gaia DR2 (Lemon et al. 2019), and PS1J1640+1932 ($p_{CNN} = 1.0$ and grade of 2.25) from SDSS (Wang et al. 2017).

Postage stamps of the 335 newly-discovered and 23 published galaxy-scale lens candidates from our Pan-STARRS CNN search are shown in Fig. 9 and in Appendix A, together with p_{CNN} and visual inspection grades. Given that some visual identifications rely on Legacy imaging, which is sometimes deeper than PS1, we also show Legacy 3-color images of our candidates located in the Legacy footprint in Appendix A.

---

[12] https://www.ast.cam.ac.uk/ioa/research/lensedquasars/
[13] http://simbad.u-strasbg.fr/simbad/sim-fcoo
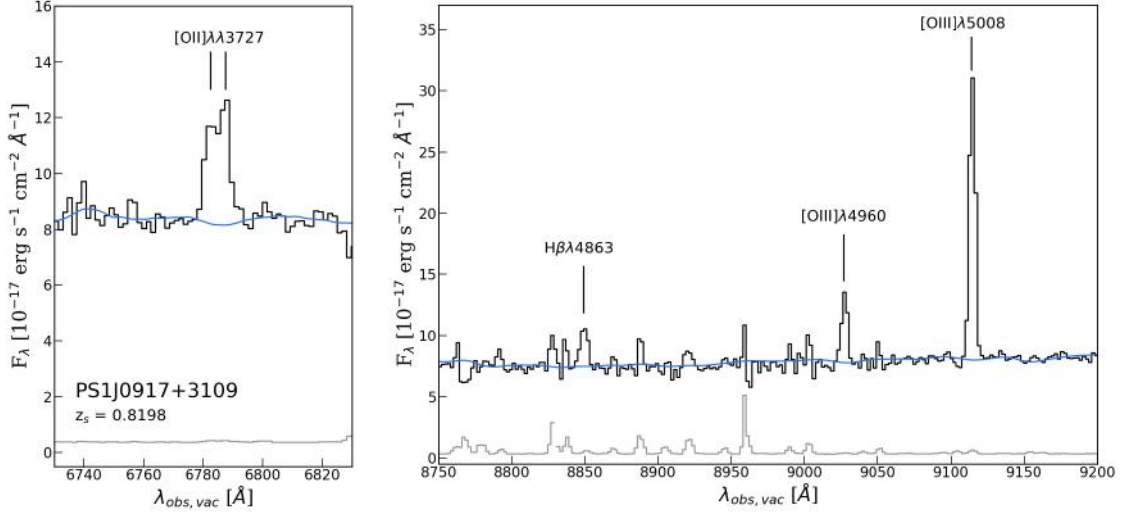
Fig. 11. Example of a lens candidate with multiple emission lines from a high-redshift background galaxy overlaid on the SDSS BOSS spectrum of the foreground LRG. The black, grey and blue lines show the observed spectrum, the 1σ noise level, and the best-fit SDSS template for the LRG, respectively. The spectrum is zoomed on the spectral features associated with the background line-emitter at $z = 0.8198$ rather than with the LRG at $z = 0.2386$.

6.2. Ancillary spectroscopy

We inspect SDSS BOSS spectra from the 16th data release available for 104 out of 358 lens candidates, in order to characterize the candidate lens galaxies and to search for spectral signatures of high-redshift background galaxies. This approach was previously used to select the SLACS sample (Bolton et al. 2008) and relies on spectral features captured within the small, 2″ diameter aperture fibers. Our examination results in:

- 84 spectra of typical LRGs at intermediate redshift with bright continuum, prominent 4000Å break, deep stellar absorption lines, and non- or very faint [OII]$\lambda\lambda3727$ detections indicating evolved stellar populations with little residual star formation.
- Seven LRG-like spectra with two or more emission and/or absorption lines falling at a different and concordant redshift, higher than the LRG redshift, and indicating the presence of a background galaxy. Two of them are already published as confirmed strong lens systems: PS1J2343−0030 as part of the SLACS sample (Auger et al. 2009), and PS1J1640+1932 (lensed quasar from Wang et al. 2017).
- Eight LRG-like spectra overlaid with a single bright, high-redshift emission line consistent with [OII]$\lambda\lambda3727$ from a background star-forming galaxy at $0.95 < z < 1.50$. Although the line widths and resolved double-peaked profiles are those expected for the [OII] doublet, other bright emission lines (H$\beta\lambda4863$, [OIII]$\lambda4960$ and [OIII]$\lambda5008$) are redshifted out of the BOSS spectral window and we consider these identifications as ambiguous.
- Three cases showing clear signatures of star-forming galaxies at $z < 0.3$, which likely have blue arms misidentified as lensed arcs, one QSO at $z = 0.5890$, and one star. These five systems are considered as false positives.

Finding a vast majority of LRGs[14] and only 3/104 star-forming galaxies at lower redshift demonstrates the validity of our method. This result shows that our CNN and visual inspection

method predominantly selects the targeted population of galaxy-scale strong lens candidates with lens LRGs, and efficiently distinguishes strong lensing features from usual interlopers (e.g., spiral arms, tidal features, blue rings). Moreover, the five false positives (PS1J2249+3228, PS1J1551+2156, PS1J1452+1047, PS1J0834+1443, and the QSO PS1J1156+5032) are all listed as lower confidence candidates with grades ≤ 2.25.

The rarity of spectroscopic signatures from lensed galaxies is not surprising because the 2″ BOSS fibers enclose little lensed source emission in the $\theta_{\rm E} \gtrsim 1.5''$ systems targeted by our search. Background line flux can only be detected in few favorable cases, like in the presence of counter-images closer to the lens center. In addition, emission lines in most lensed galaxies might be too faint for SDSS spectroscopy, and the observable spectral band of BOSS excludes H$\beta4863$, [OIII]4960 and [OIII]5008 for $z > 0.9$, which rules out multiple line detections for the majority of sources expected at $z > 1$.

The only Pan-STARRS candidate robustly confirmed as a strong lens system is PS1J1415+1112. Pan-STARRS imaging spatially resolves the system into a quadruply-imaged background source forming a typical fold configuration, and with redder color than the lens LRG (Fig. 9). The best-fit model from the BOSS pipeline primarily identifies spectral features from the foreground LRG at $z_{\rm d} = 0.3155$, but poorly fits the continuum and remarkably prominent Balmer absorption lines at $\lambda_{\rm obs} > 8000$ Å (Fig. 10). These features are associated with the background galaxy at $z_{\rm s} = 1.185$. Further inspection of the BOSS spectrum shows that the strong Balmer absorption lines, together with the weak 4000 Å break indicative of relatively young stellar populations, and the lack of nebular emission lines at $z_{\rm s} = 1.185$ suggesting little on-going star formation, favor the scenario of a recently quenched galaxy. To verify this hypothesis, we use the BC03 stellar population synthesis models (Bruzual & Charlot 2003) to combine the SED template of an elliptical galaxy at $z_{\rm d} = 0.3155$ with 7 Gyr old stellar populations and solar metallicity with various templates of post-starbursts at $z_{\rm s} = 1.185$. After varying the stellar age, metallicity, and dust attenuation, we find that rescaling the SED of a young galaxy with 25 Myr old stellar populations, no on-going star formation, and $Z = 0.2$ Z$_\odot$ correctly fits the overall wavelength range in Fig. 10. Together with

---

[14] Although we can not completely rule out that in few cases, these are actually the central bulges of late-type galaxies covered by BOSS.

the red colors of multiple images this adds further evidence that the lensed galaxy has indeed ceased star formation recently.

The last four CNN candidates showing multiple emission lines from a background, possibly lensed galaxy do not exhibit such clear configurations in Pan-STARRS and Legacy *gri* images. Their BOSS spectra reveal simultaneous detections of [OII]$\lambda\lambda3727$, H$\beta\lambda4863$, [OIII]$\lambda4960$, and [OIII]$\lambda5008$ on top of the prominent stellar continuum from the foreground LRG (see Fig. 11). The first three are PS1J2345−0209 with $z_{\rm LRG} = 0.2940$ and $z_{\rm s} = 0.6581$, PS1J1134+1712 with $z_{\rm LRG} = 0.3752$ and $z_{\rm s} = 0.8121$, and PS1J0917+3109 with $z_{\rm LRG} = 0.2386$ and $z_{\rm s} = 0.8198$. These candidates were listed as probable lenses from our grades and, although $z_{\rm LRG}$, $z_{\rm s}$, and $\sigma^*_{\rm LRG}$ suggest plausible Einstein radii $\sim 1''$ for singular isothermal sphere profiles, high-resolution follow-up imaging is needed to ascertain their configuration. These data will determine whether the background, spectroscopically-confirmed galaxies are those visually identified with Pan-STARRS and indeed multiply-imaged, or whether they are out of the strong lensing regime. Lastly, PS1J1724+3146 comprises a foreground LRG at $z_{\rm LRG} = 0.2097$ and a background source at $z_{\rm s} = 0.3461$, likely too close to the lens to enter the strong lensing regime.

6.3. Properties of candidates

Our visual inspection stage implies that resulting lens candidates have morphologies and configurations easily detectable by the human eye. Figure 9 confirms that higher grades are given to systems with extended arcs, clear counter images and often compact lens light profiles. Postage stamps make it clear that our most reliable systems have relatively brighter and distorted arcs (as plausible strongly lensed background galaxies) in *gri* bands which will facilitate their future follow-up. Interestingly, besides the numerous blue arcs (e.g., PS1J1647+1117, PS1J1508−1652), several candidates have lensed sources redder than the foreground LRGs (e.g., PS1J1559−3147, PS1J1445+3649) and others have compact, nearly point-like morphologies suggestive of lensed quasars (e.g., PS1J1926−2138). Since the presence of possible counter images is a prerequisite for lens identifications, our candidate set is presumably biased towards higher fractions of quads than doubles, at least for grades ~ 3. Other biases on the relative positions of lenses and sources might also arise. For instance, although our tests suggest that systems with $\theta_{\rm E}/R_{\rm eff} < 1$ are correctly classified by the CNN, with only minor differences in $p_{\rm CNN}$ with respect to $\theta_{\rm E}/R_{\rm eff} > 1$ (Fig. 7), candidates and known lenses recovered by visual inspection should be relatively less blended and lie on the high-end of the $\theta_{\rm E}/R_{\rm eff}$ distribution. Quantifying this effect is nevertheless an arduous task due to uncertainties in reliably measuring $R_{\rm eff}$ from Pan-STARRS imaging. As previously mentioned, systems with $\theta_{\rm E}$ differing from simulated lenses in our training set are likely all discarded.

Our 358 candidates have lens redshifts in the range $z_{\rm d} \sim 0.15$–0.65. The distribution does not change much between candidates with confirmed lens $z_{\rm spec}$ from SDSS, and those with more uncertain SDSS $z_{\rm phot}$ due to lens/source blending. It closely matches the lens redshift ranges in other samples selected through multiband, ground-based imaging such as CASSOWARY (Stark et al. 2013) and SL2S (Sonnenfeld et al. 2013). Interestingly, Pan-STARRS candidates with SDSS stellar velocity dispersion have $\sigma^*_{\rm mean} \sim 275$ km s^{-1}. This is significantly lower than $\sigma^*_{\rm mean} \sim 310$ km s^{-1} in the set of LRGs for

simulations (Sect. 4.4), indicating that lens LRGs in our candidate set are less massive on average.

To understand implications of such differences in σ^* we followed Petrillo et al. (2017) and, for each lens candidate with $z_{\rm d}$ and σ^* available from BOSS, we calculated Einstein radii for a singular isothermal sphere profile and different source redshifts spanning the most plausible $z_{\rm s} = 0.5$–3.0 range. We assumed $\sigma_{\rm SIS} \sim \sigma^*$. In the vast majority of cases (86%), Einstein radii predicted from the lens galaxy dynamics match the approximate $\theta_{\rm E} \sim 1$–$2''$ of PS1 candidates from a basic inspection of 3-color images in Fig. 9. This range is also expected from construction of the training set and our CNN selection function. Predicted and observed image configurations usually match for $z_{\rm s} > 1$. This qualitative test argues in favour of plausible lens configurations and few contaminants despite the moderate σ^* from BOSS.

In some cases, the large Einstein radii $\gtrsim 1.5''$ are likely to be partly attributed to a contribution from the environment of the primary lens galaxy, probably from a smooth dark-matter halo associated with an extended group- or cluster-scale structure (Oguri 2006). As a matter of fact, obtaining a few strong lens candidates with $\theta_{\rm E}$ in the same range as our lens simulations but with lower SDSS stellar velocity dispersions proves that, if they are genuine strong lenses, they host moderately massive lens LRGs with significant external shear and magnification contributions from the environment. We verified that some of our Pan-STARRS candidates are indeed matching the position of the central brightest cluster galaxy of SDSS clusters (e.g., PS1J0907+4233, PS1J2153+1154, PS1J1417+2120, PS1J1210+2843, PS1J1730+3405, Szabo et al. 2011), and of candidate galaxy clusters from a red sequence search in DES imaging (e.g., PS1J0919+0336, PS1J2233+3012, PS1J1210+2843, PS1J1414+6447, Rykoff et al. 2016). This environmental effect is well illustrated by the case of PS1J0454−0308 characterized in Schirmer et al. (2010). We also found that PS1J2210+0620 and its bright red arc of ∼8″ extension lie behind the core of Abell 2422 galaxy cluster (Abell et al. 1989). Lastly, PS1J1142+5830 is located in the field of the rich, X-ray luminous galaxy cluster MACSJ1142.4+5831 at $z = 0.325$, also known as Abell 1351, which has a bimodal velocity distribution suggesting an on-going merger (Barrena et al. 2014). The SDSS photo-z of PS1J1142+5830 is consistent with the cluster redshift but our candidate is offset by 1.3′ from the brightest cluster galaxy.

The Pan-STARRS *gri* photometry of our 358 candidates is comparable to that of our lens simulations. Observed $(g - i)$ colors of the deflector central regions within 2″ diameter apertures range between 1.3 and 2.7 mag and broadly follow the color distribution of mocks and $p_{\rm cat} > 0.5$ galaxies in Fig. 2. Our best candidates are therefore representative of the global sample and visual inspection does not introduce significant biases in terms of lens color. Kron $(g - i)$ colors from blended deflector and source emissions are ∼0.3 mag lower because lensed arcs are predominantly bluer than the lens LRGs. Given uncertainties on the lensed source colors, quantitative analyses would require subtracting the lens LRG light profile, a hazardous task with Pan-STARRS imaging. However, it is worth noting that a majority of $p_{\rm CNN} > 0.9$ systems with blue arcs closely mimicking extended arms of star-forming spirals were conservatively discarded by visual inspection, while systems with similar configurations but redder arcs where considered less ambiguous and assigned higher grades. Consequently, the output set is likely biased towards a higher fraction of red lensed arcs compared to all genuine lens systems assigned $p_{\rm CNN} > 0.9$.

We did not find significant correlations between average grades and photometric properties. Although our high and lower-confidence candidates have comparable lens brightness, those with higher grades have slightly redder lenses by ~0.15 mag in $(g − i)$ on average. Mean lens redshifts and velocity dispersions are also increasing in the top half of the candidate set, by 0.05 and 50 km s^{-1}, respectively.

6.4. Discussion

Our study demonstrates that a two-step approach combining catalog-level and image-level classifications, as already applied to lensed quasars searches (Agnello et al. 2015), is efficient in selecting galaxy-scale strong lenses from very wide-field surveys without imposing restrictive cuts on the input galaxy catalog. Using three bands and multi-aperture photometry, our catalog-level neural network conveniently reduces the sample size for CNN classification to the order of 1 million sources which, in the case of Pan-STARRS, allows us to download all *gri* cutouts within a manageable amount of time of about one week. This first stage will be particularly beneficial to overcome data volume limitations in the new era of deep, large scale surveys such as LSST. At the same time, the low false negative rate and good performance on known lens systems of our catalog-level network applied to Pan-STARRS photometry shows that this stage discards very few potentially interesting systems. After that, we obtain encouraging results from our CNN combined with visual inspection. The compilation of 330 newly-discovered lens candidates (after removing the five false-positives identified from SDSS BOSS spectra) and confirmation of 23 lenses already selected from other, more suitable surveys (e.g., DES, KiDS) demonstrates the efficiency of our approach regardless of the limited depth and seeing in Pan-STARRS.

The strategy presented in this paper is expected to be easily applicable to the deeper LSST *gri* stacks in order to identify the large set of new, wide-separation galaxy-scale lenses from this survey. The simulations of Collett (2015) suggest that the LSST final stacks in *gri* bands will yield about 39 000 detectable lens systems, with θ_E greater than the seeing FWHM and large enough to spatially-resolve multiple images, and with total S/N of lensed arcs > 20 in at least one band. Under these assumptions, future LSST lenses will mainly cover $\theta_E = 1–3''$, a similar range as our Pan-STARRS candidates, and their systematic identification will be crucial for several science cases including the search for strongly lensed SNe with spatially-resolved multiple images for early-phase SN spectroscopy and cosmography (Suyu et al. 2020). In order to achieve this, we can customize our simulation pipeline of realistic Pan-STARRS mock lenses to produce LSST mocks and quickly assemble a training set, by using *gri* cutouts of the relevant LRG lenses from LSST stacks rather than Pan-STARRS. Extending the search to broader populations of lens galaxies might also become feasible, in light of the ~4 mag deeper *gri* LSST stacks.

Tests on the CNN performance presented in this paper are likely valid essentially for Pan-STARRS seeing and depth, while better imaging quality should enable identifications of broader, more complex image patterns and would likely benefit from updates on the neural network. The main challenge is the minimization of false positives which, given the rarity of strong lenses per deg^2, will largely dominate the sample of CNN candidates even with FPR down to 1% or less. Potential avenues for improvements include adding other convolutional layers or boosting the learning process with residual networks (He et al. 2015), as the latter might give better performance for image features not represented in the training data (for LSST simulations, see Lanusse et al. 2018). A possibility would be to use CNNs optimized for image outlier detection (e.g., Margalef-Bentabol et al. 2020), either to identify strong lenses as the outlier class, or simply to exclude cutouts with partial coverage, background artifacts or other anomalies before classification. In addition, although Teimoorinia et al. (2020) found little difference with single-band HST images, implementing additional classes for the usual interlopers (spirals, ring galaxies, ...) might help distinguish signatures of strong lenses in *gri* bands. Our Pan-STARRS lens search demonstrates that ultimately, most progress should come from the choice of positive and negative examples in the training set (see Sect. 5.5). Highly-realistic lens simulations are one of the main ingredients (see Lanusse et al. 2018). For instance, as multiple images are strongly blended with lenses in about half of the mocks produced in Sect. 4.4, one could only include those visually classified as definite lenses from their bright arcs and unambiguous configurations. Fine-tuning the selection of positive examples in this way could help the network assign high scores exclusively to robust candidates that are worth including for follow-up campaigns.

Reducing the false positive rates and making sure that only high-confidence candidates get $p_{CNN} \sim 1$ will be crucial for future lens searches in the LSST era. However, the most efficient neural networks should provide orders of magnitudes more lens candidates than Pan-STARRS and their systematic visual inspection might become unrealistic. Assembling complete strong lens samples will therefore require one to abandon this non-automated, human-classification stage and to search for alternatives. For instance, calibrating the CNN scores as probabilities (e.g., Guo et al. 2017) could help quantify purity and completeness, and automatically select a subset of candidates for high-resolution imaging or spectroscopic follow-up.

7. Conclusion

In this paper, we present a systematic search for wide-separation, galaxy-scale strong lenses in Pan-STARRS using machine learning classification of *gri* images from the 3π survey on the entire northern sky. We focused our search on massive LRGs acting as strong lenses and producing Einstein radii $\geq 1.5''$, and we simulated a set of highly-realistic mocks by painting lensed arcs on Pan-STARRS image cutouts of LRGs with known redshift and velocity dispersion from SDSS. This strategy ensures that mocks include background artifacts and field galaxies, and that the network becomes invariant under the small scale exposure and FWHM variations on the survey stacks.

We computed the *gri* aperture photometry of mocks to preselect a conservative catalog of 23.1 million sources, and followed a two-step approach for classification: (1) a catalog-based neural network on the source photometry, (2) a CNN trained on *gri* image cutouts. The catalog-level network assigned $p_{cat} > 0.5$ for 1 050 207 galaxies while excluding little known lenses from the MasterLens catalog. The image-level network then yielded sets of 105 760 and 12 382 candidates with scores $p_{CNN} > 0.5$ and > 0.9, respectively. We visually inspected those with $p_{CNN} > 0.9$ and combined with previous CNNs to assemble a final set of 330 high-quality newly-discovered candidates with average visual grades ≥ 2. Publicly available BOSS spectroscopy of the lens candidates' central regions proves that the vast majority are indeed LRGs at $z \sim 0.1–0.7$, and five newly-discovered candidates show robust signatures of blended, high-redshift background sources. Pan-STARRS clearly resolves one of them as

a quadruply-imaged red galaxy at $z_s = 1.185$ (likely recently quenched), behind a lens LRG at $z_d = 0.3155$.

This new set of bright lens candidates is particularly valuable for future lensed SNe searches. Strong lenses with such image separations are indeed likely to produce long time delays of a few days to weeks which alleviates difficulties affecting $\theta_E < 1''$ lensed SNe such as iPTF16geu and allows one to measure accurate, microlensing-free time delays for cosmography. Such time delays are also well-suited to trigger timely imaging and spectroscopic follow-up of a SN reappearance to characterize the SN's early-phase behaviour within a few days after explosion. In the meantime, validating these Pan-STARRS lens candidates and deriving strong lensing models will require high-resolution imaging and/or spectroscopic follow-up.

Our CNN exhibits good performance on known lenses detected in Pan-STARRS, correctly classifying 14/16 systems as lenses and assigning scores $p_{CNN} > 0.9$ to 7/16. We found that CNN predictions strongly depend on the construction of the training set but little on the network architecture. Our search also recovered 23 confirmed or candidate strong lenses in the literature out of the MasterLens catalog. In the near future, the release of deep stacks with best seeing conditions in smaller fields as part of Pan-STARRS DR3 will give the opportunity to extend our search to optimal PS1 data quality. In addition, we expect that the efficient and automated two-step classification method presented in this paper will be applicable to the deep *gri* image stacks from LSST with only minor adjustments.

Acknowledgements

References

Abell, G. O., Corwin, Harold G., J., & Olowin, R. P. 1989, ApJS, 70, 1
Agnello, A., Kelly, B. C., Treu, T., & Marshall, P. J. 2015, MNRAS, 448, 1446
Aihara, H., AlSayyad, Y., Ando, M., et al. 2019, PASJ, 106
Aihara, H., Armstrong, R., Bickerton, S., et al. 2018, PASJ, 70, S8
Auger, M. W., Budzynski, J. M., Belokurov, V., Koposov, S. E., & McCarthy, I. G. 2013, MNRAS, 436, 503
Auger, M. W., Treu, T., Bolton, A. S., et al. 2009, ApJ, 705, 1099
Avestruz, C., Li, N., Zhu, H., et al. 2019, ApJ, 877, 58
Barnabè, M., Czoske, O., Koopmans, L. V. E., Treu, T., & Bolton, A. S. 2011, MNRAS, 415, 2215
Barnabè, M., Spiniello, C., Koopmans, L. V. E., et al. 2013, MNRAS, 436, 253
Barrena, R., Girardi, M., Boschin, W., De Grandi, S., & Rossetti, M. 2014, MNRAS, 442, 2216
Bautista, J. E., Vargas-Magaña, M., Dawson, K. S., et al. 2018, ApJ, 863, 110
Berghea, C. T., Nelson, G. J., Rusu, C. E., Keeton, C. R., & Dudik, R. P. 2017, ApJ, 844, 90
Bertin, E. & Arnouts, S. 1996, A&AS, 117, 393
Bertin, E., Mellier, Y., Radovich, M., et al. 2002, Astronomical Society of the Pacific Conference Series, Vol. 281, The TERAPIX Pipeline, ed. D. A. Bohlender, D. Durand, & T. H. Handley, 228
Bolton, A. S., Burles, S., Koopmans, L. V. E., et al. 2008, ApJ, 682, 964
Bonvin, V., Courbin, F., Suyu, S. H., et al. 2017, MNRAS, 465, 4914
Bonvin, V., Tihhonova, O., Millon, M., et al. 2019, A&A, 621, A55
Bruzual, G. & Charlot, S. 2003, MNRAS, 344, 1000
Buckley-Geer, E. J., Lin, H., Rusu, C., et al. 2020, arXiv e-prints, arXiv:2003.12117
Cañameras, R., Nesvadba, N., Kneissl, R., et al. 2017a, A&A, 604, A117
Cañameras, R., Nesvadba, N. P. H., Kneissl, R., et al. 2017b, A&A, 600, L3
Cabanac, R. A., Alard, C., Dantel-Fort, M., et al. 2007, A&A, 461, 813
Cava, A., Schaerer, D., Richard, J., et al. 2018, Nature Astronomy, 2, 76
Chambers, K. C., Magnier, E. A., Metcalfe, N., et al. 2016, arXiv e-prints, arXiv:1612.05560
Chan, J. H. H., Suyu, S. H., Sonnenfeld, A., et al. 2019, arXiv e-prints, arXiv:1911.02587
Cheng, T.-Y., Li, N., Conselice, C. J., et al. 2019, arXiv e-prints, arXiv:1911.04320
Collett, T. E. 2015, ApJ, 811, 20
Comparat, J., Richard, J., Kneib, J.-P., et al. 2015, A&A, 575, A40
Courbin, F., Bonvin, V., Buckley-Geer, E., et al. 2018, A&A, 609, A71
Danielson, A. L. R., Swinbank, A. M., Smail, I., et al. 2011, MNRAS, 410, 1687
Davies, A., Serjeant, S., & Bromley, J. M. 2019, MNRAS, 487, 5263
Dawson, K. S., Schlegel, D. J., Ahn, C. P., et al. 2013, AJ, 145, 10
de Jong, J. T. A., Verdoes Kleijn, G. A., Kuijken, K. H., & Valentijn, E. A. 2013, Experimental Astronomy, 35, 25
Dey, A., Schlegel, D. J., Lang, D., et al. 2019, AJ, 157, 168
Dhawan, S., Johansson, J., Goobar, A., et al. 2020, MNRAS, 491, 2639
Diehl, H. T., Buckley-Geer, E. J., Lindgren, K. A., et al. 2017, ApJS, 232, 15
Dieleman, S., Willett, K. W., & Dambre, J. 2015, MNRAS, 450, 1441
Eisenstein, D. J., Annis, J., Gunn, J. E., et al. 2001, AJ, 122, 2267
Falco, E. E., Gorenstein, M. V., & Shapiro, I. I. 1985, ApJ, 289, L1

Farrow, D. J., Cole, S., Metcalfe, N., et al. 2014, MNRAS, 437, 748
Faure, C., Kneib, J.-P., Covone, G., et al. 2008, ApJS, 176, 19
Flewelling, H. A., Magnier, E. A., Chambers, K. C., et al. 2016, arXiv e-prints, arXiv:1612.05243
Freedman, W. L., Madore, B. F., Hatt, D., et al. 2019, ApJ, 882, 34
Freedman, W. L., Madore, B. F., Hoyt, T., et al. 2020, ApJ, 891, 57
Gavazzi, R., Marshall, P. J., Treu, T., & Sonnenfeld, A. 2014, ApJ, 785, 144
Gavazzi, R., Treu, T., Rhodes, J. D., et al. 2007, ApJ, 667, 176
Goldstein, D. A. & Nugent, P. E. 2017, ApJ, 834, L5
Goldstein, D. A., Nugent, P. E., Kasen, D. N., & Collett, T. E. 2018, ApJ, 855, 22
Goobar, A., Amanullah, R., Kulkarni, S. R., et al. 2017, Science, 356, 291
Griffith, R. L., Cooper, M. C., Newman, J. A., et al. 2012, ApJS, 200, 9
Grillo, C., Gobat, R., Lombardi, M., & Rosati, P. 2009, A&A, 501, 461
Grillo, C., Rosati, P., Suyu, S. H., et al. 2018, ApJ, 860, 94
Grillo, C., Rosati, P., Suyu, S. H., et al. 2020, arXiv e-prints, arXiv:2001.02232
Grogin, N. A., Kocevski, D. D., Faber, S. M., et al. 2011, ApJS, 197, 35
Guo, C., Pleiss, G., Sun, Y., & Weinberger, K. Q. 2017, in Proceedings of Machine Learning Research, Vol. 70, Proceedings of the 34th International Conference on Machine Learning, ed. D. Precup & Y. W. Teh (International Convention Centre, Sydney, Australia: PMLR), 1321–1330
Hakobyan, A. A., Adibekyan, V. Z., Aramyan, L. S., et al. 2012, A&A, 544, A81
Halkola, A., Seitz, S., & Pannella, M. 2007, ApJ, 656, 739
Hasinger, G., Capak, P., Salvato, M., et al. 2018, ApJ, 858, 77
He, K., Zhang, X., Ren, S., & Sun, J. 2015, arXiv e-prints, arXiv:1512.03385
Hezaveh, Y. D., Dalal, N., Marrone, D. P., et al. 2016, ApJ, 823, 37
Huang, X., Domingo, M., Pilon, A., et al. 2019, arXiv e-prints, arXiv:1906.00970
Huber, S., Suyu, S. H., Noebauer, U. M., et al. 2019, A&A, 631, A161
Ioffe, S. & Szegedy, C. 2015, in Proceedings of the 32nd International Conference on International Conference on Machine Learning - Volume 37, ICML15 (JMLR.org), 448456
Ivezić, Ž., Kahn, S. M., Tyson, J. A., et al. 2019, ApJ, 873, 111
Jacobs, C., Collett, T., Glazebrook, K., et al. 2019a, ApJS, 243, 17
Jacobs, C., Collett, T., Glazebrook, K., et al. 2019b, MNRAS, 484, 5330
Jacobs, C., Glazebrook, K., Collett, T., More, A., & McCarthy, C. 2017, MNRAS, 471, 167
Jaelani, A. T., More, A., Oguri, M., et al. 2020, arXiv e-prints, arXiv:2002.01611
Kelly, P. L., Rodney, S. A., Treu, T., et al. 2015, Science, 347, 1123
Koekemoer, A. M., Aussel, H., Calzetti, D., et al. 2007, ApJS, 172, 196
Koekemoer, A. M., Faber, S. M., Ferguson, H. C., et al. 2011, ApJS, 197, 36
Koopmans, L. V. E., Bolton, A., Treu, T., et al. 2009, ApJ, 703, L51
Laigle, C., McCracken, H. J., Ilbert, O., et al. 2016, ApJS, 224, 24
Lanusse, F., Ma, Q., Li, N., et al. 2018, MNRAS, 473, 3895
Lasker, B. M., Lattanzi, M. G., McLean, B. J., et al. 2008, AJ, 136, 735
Le Fèvre, O., Tasca, L. A. M., Cassata, P., et al. 2015, A&A, 576, A79
Leauthaud, A., Massey, R., Kneib, J.-P., et al. 2007, ApJS, 172, 219
LeCun, Y., Bengio, Y., & Hinton, G. 2015, Nature, 521, 436
LeCun, Y., Bottou, L., Bengio, Y., & Haffner, P. 1998, in Proceedings of the IEEE, 2278–2324
Lemon, C. A., Auger, M. W., & McMahon, R. G. 2019, MNRAS, 483, 4242
Li, R., Napolitano, N. R., Tortora, C., et al. 2020, arXiv e-prints, arXiv:2004.02715
Lilly, S. J., Le Fèvre, O., Renzini, A., et al. 2007, ApJS, 172, 70
Lintott, C., Schawinski, K., Bamford, S., et al. 2011, MNRAS, 410, 166
Lintott, C. J., Schawinski, K., Slosar, A., et al. 2008, MNRAS, 389, 1179
M. Green, G. 2018, The Journal of Open Source Software, 3, 695
Magnier, E. A., Sweeney, W. E., Chambers, K. C., et al. 2016, arXiv e-prints, arXiv:1612.05244
Margalef-Bentabol, B., Huertas-Company, M., Charnock, T., et al. 2020, arXiv e-prints, arXiv:2003.08263
Marshall, P. J., Hogg, D. W., Moustakas, L. A., et al. 2009, ApJ, 694, 924
Marshall, P. J., Verma, A., More, A., et al. 2016, MNRAS, 455, 1171
Masci, F. J., Laher, R. R., Rusholme, B., et al. 2019, PASP, 131, 018003
Metcalf, R. B., Meneghetti, M., Avestruz, C., et al. 2019, A&A, 625, A119
Millon, M., Galan, A., Courbin, F., et al. 2019, arXiv e-prints, arXiv:1912.08027
More, A., Suyu, S. H., Oguri, M., More, S., & Lee, C.-H. 2017, ApJ, 835, L25
More, A., Verma, A., Marshall, P. J., et al. 2016, MNRAS, 455, 1191
Nair, V. & Hinton, G. E. 2010, in ICML, ed. J. Frnkranz & T. Joachims (Omnipress), 807–814
Oguri, M. 2006, MNRAS, 367, 1241
Oguri, M. & Marshall, P. J. 2010, MNRAS, 405, 2579
Petrillo, C. E., Tortora, C., Chatterjee, S., et al. 2017, MNRAS, 472, 1129
Petrillo, C. E., Tortora, C., Vernardos, G., et al. 2019, MNRAS
Planck Collaboration. 2018, Planck 2018 results. VI. Cosmological parameters
Planck Collaboration XIII. 2016, A&A, 594, A13
Prakash, A., Licquia, T. C., Newman, J. A., et al. 2016, ApJS, 224, 34

Ranzato, M. A., Boureau, Y.-L., & LeCun, Y. 2007, in Proceedings of the 20th International Conference on Neural Information Processing Systems, NIPS07 (Red Hook, NY, USA: Curran Associates Inc.), 11851192
Riess, A. G., Casertano, S., Yuan, W., Macri, L. M., & Scolnic, D. 2019, ApJ, 876, 85
Ritondale, E., Vegetti, S., Despali, G., et al. 2019, MNRAS, 485, 2179
Rumelhart, D. E., Hinton, G. E., & Williams, R. J. 1986, Nature, 323, 533
Russakovsky, O., Deng, J., Su, H., et al. 2015, International Journal of Computer Vision (IJCV), 115, 211
Rusu, C. E., Berghea, C. T., Fassnacht, C. D., et al. 2019, MNRAS, 486, 4987
Rykoff, E. S., Rozo, E., Hollowood, D., et al. 2016, ApJS, 224, 1
Schaefer, C., Geiger, M., Kuntzer, T., & Kneib, J. P. 2018, A&A, 611, A2
Schirmer, M., Suyu, S., Schrabback, T., et al. 2010, A&A, 514, A60
Schlafly, E. F. & Finkbeiner, D. P. 2011, ApJ, 737, 103
Schlegel, D., White, M., & Eisenstein, D. 2009, in astro2010: The Astronomy and Astrophysics Decadal Survey, Vol. 2010, 314
Schlegel, D. J., Finkbeiner, D. P., & Davis, M. 1998, ApJ, 500, 525
Schuldt, S., Chirivì, G., Suyu, S. H., et al. 2019, A&A, 631, A40
Scoville, N., Abraham, R. G., Aussel, H., et al. 2007, ApJS, 172, 38
Secrest, N. J., Dudik, R. P., Dorland, B. N., et al. 2015, ApJS, 221, 12
Shajib, A. J., Birrer, S., Treu, T., et al. 2020, MNRAS
Shu, Y., Bolton, A. S., Brownstein, J. R., et al. 2015, ApJ, 803, 71
Silverman, J. D., Kashino, D., Sanders, D., et al. 2015, ApJS, 220, 12
Simmons, B. D., Lintott, C., Willett, K. W., et al. 2017, MNRAS, 464, 4420
Sonnenfeld, A., Chan, J. H. H., Shu, Y., et al. 2018, PASJ, 70, S29
Sonnenfeld, A., Gavazzi, R., Suyu, S. H., Treu, T., & Marshall, P. J. 2013, ApJ, 777, 97
Sonnenfeld, A., Jaelani, A. T., Chan, J., et al. 2019, A&A, 630, A71
Sonnenfeld, A., Treu, T., Marshall, P. J., et al. 2015, ApJ, 800, 94
Sonnenfeld, A., Verma, A., More, A., et al. 2020, arXiv e-prints, arXiv:2004.00634
Srivastava, N., Hinton, G., Krizhevsky, A., Sutskever, I., & Salakhutdinov, R. 2014, Journal of Machine Learning Research, 15, 1929
Stark, D. P., Auger, M., Belokurov, V., et al. 2013, MNRAS, 436, 1040
Suyu, S. H., Bonvin, V., Courbin, F., et al. 2017, MNRAS, 468, 2590
Suyu, S. H. & Halkola, A. 2010, A&A, 524, A94
Suyu, S. H., Hensel, S. W., McKean, J. P., et al. 2012, ApJ, 750, 10
Suyu, S. H., Huber, S., Cañameras, R., et al. 2020, arXiv e-prints, arXiv:2002.08378
Szabo, T., Pierpaoli, E., Dong, F., Pipino, A., & Gunn, J. 2011, ApJ, 736, 21
Tanaka, M., Hasinger, G., Silverman, J. D., et al. 2017, arXiv e-prints, arXiv:1706.00566
Tasca, L. A. M., Le Fèvre, O., Ribeiro, B., et al. 2017, A&A, 600, A110
Teimoorinia, H., Toyonaga, R. D., Fabbro, S., & Bottrell, C. 2020, PASP, 132, 044501
Tonry, J. & Onaka, P. 2009, in Advanced Maui Optical and Space Surveillance Technologies Conference, E40
Treu, T. & Koopmans, L. V. E. 2002, ApJ, 575, 87
Turner, E. L., Ostriker, J. P., & Gott, J. R., I. 1984, ApJ, 284, 1
Tutukov, A. V. & Yungelson, L. R. 1981, Nauchnye Informatsii, 49, 3
Vegetti, S., Lagattuta, D. J., McKean, J. P., et al. 2012, Nature, 481, 341
Wang, L., Shu, Y., Li, R., et al. 2017, MNRAS, 468, 3757
Waters, C. Z., Magnier, E. A., Price, P. A., et al. 2016, arXiv e-prints, arXiv:1612.05245
Whelan, J. & Iben, Icko, J. 1973, ApJ, 186, 1007
Willett, K. W., Galloway, M. A., Bamford, S. P., et al. 2017, MNRAS, 464, 4176
Willett, K. W., Lintott, C. J., Bamford, S. P., et al. 2013, MNRAS, 435, 2835
Wojtak, R., Hjorth, J., & Gall, C. 2019, MNRAS, 487, 3342
Wong, K. C., Sonnenfeld, A., Chan, J. H. H., et al. 2018, ApJ, 867, 107
Wong, K. C., Suyu, S. H., Chen, G. C. F., et al. 2019, arXiv e-prints, arXiv:1907.04869
Yahalomi, D. A., Schechter, P. L., & Wambsganss, J. 2017, arXiv e-prints, arXiv:1711.07919

Appendix A: Complete list of candidates

[1] Max-Planck-Institut für Astrophysik, Karl-Schwarzschild-Str. 1, 85748 Garching, Germany
e-mail: rcanameras@mpa-garching.mpg.de
[2] Physik Department, Technische Universität München, James-Franck Str. 1, 85741 Garching, Germany
[3] Institute of Astronomy and Astrophysics, Academia Sinica, 11F of ASMAB, No.1, Section 4, Roosevelt Road, Taipei 10617, Taiwan

Name	RA	Dec	p_{CNN}	Grade	g_{Kron}	r_{Kron}	i_{Kron}	g_{aper}	r_{aper}	i_{aper}	Redshift	Notes
PS1J0454−0016	04:54:03	−00:16:15	0.981	2.75	20.84	19.54	18.89	22.33	20.89	20.02	0.39	
PS1J0454−0308	04:54:01	−03:08:34	1.000	2.75	19.16	17.77	17.14	20.96	19.52	18.92	...	(m)
PS1J0354−2420	03:54:47	−24:20:15	0.943	2.75	21.26	20.29	19.28	23.23	21.85	20.74	...	(a)
PS1J0143+1607	01:43:50	+16:07:39	1.000	2.75	...	18.96	18.39	22.51	20.87	20.11	0.39	(g)
PS1J2355+3252	23:55:28	+32:52:45	0.951	2.50	19.49	18.42	17.88	21.41	19.71	19.01	0.53	
PS1J2343−0030	23:43:59	−00:30:22	0.917	2.50	18.44	17.31	16.82	19.84	18.71	18.22	0.1807[*]	(h)
PS1J2338−1321	23:38:45	−13:21:32	0.900	2.50	18.32	17.09	16.44	20.32	19.09	18.47	...	
PS1J2322+1821	23:22:04	+18:21:30	0.993	2.50	20.2	18.81	18.23	21.54	20.14	19.48	0.26	
PS1J2210+0620	22:10:34	+06:20:04	1.000	2.50	20.69	...	...	21.95	21.05	20.26	...	
PS1J2208+0446	22:08:05	+04:46:03	0.959	2.50	19.01	17.46	16.85	21.05	19.54	18.92	0.25	(l)
PS1J2153+1154	21:53:10	+11:54:55	1.000	2.50	19.22	17.85	17.25	20.92	19.44	18.86	0.2891[*]	
PS1J2144+2411	21:44:01	+24:11:52	0.998	2.50	...	19.64	18.83	22.53	20.92	20.09	0.34	
PS1J1903+5225	19:03:43	+52:25:06	1.000	2.50	...	20.27	19.34	23.24	21.61	20.46	...	
PS1J1841+4515	18:41:18	+45:15:41	0.931	2.50	21.47	19.78	18.92	22.91	21.21	20.28	...	
PS1J1803+7358	18:03:43	+73:58:59	1.000	2.50	16.15	15.27	14.88	18.54	17.64	17.15	...	
PS1J1723+1650	17:23:46	+16:50:13	0.998	2.50	20.02	18.52	17.62	21.34	19.96	19.16	...	
PS1J1657+3150	16:57:11	+31:50:53	0.993	2.50	...	19.83	19.23	23.1	21.61	20.75	0.5150[*]	
PS1J1650+3123	16:50:50	+31:23:28	0.997	2.50	20.64	20.21	19.55	22.13	21.58	20.76	0.6817[*]	
PS1J1603+3330	16:03:09	+33:30:36	0.971	2.50	20.91	19.87	19.11	22.36	20.95	20.17	0.4651[*]	
PS1J1527+6048	15:27:50	+60:48:05	0.953	2.50	18.75	18.4	18.2	20.53	20.01	19.63	0.10	
PS1J1422+0209	14:22:10	+02:09:09	0.954	2.50	20.46	19.02	18.08	22.08	20.43	19.58	0.4656[*]	(f)
PS1J1420+0600	14:20:52	+06:00:38	0.991	2.50	20.54	19.43	18.81	21.83	20.57	19.99	0.47	
PS1J1420+1258	14:20:39	+12:58:18	0.909	2.50	...	20.13	19.07	22.87	21.19	20.14	0.5378[*]	
PS1J1417+2120	14:17:57	+21:20:13	0.999	2.50	20.78	19.01	18.25	21.95	20.4	19.57	0.4225[*]	
PS1J1410+2418	14:10:23	+24:18:57	0.996	2.50	20.49	19.02	18.39	22.08	20.62	19.73	0.4051[*]	
PS1J1247+3644	12:47:25	+36:44:04	0.987	2.50	20.95	20.53	19.39	23.22	21.93	20.84	0.5756[*]	
PS1J1210+2843	12:10:14	+28:43:28	0.962	2.50	20.29	19.36	18.48	21.79	20.24	19.64	0.34	
PS1J1136+5214	11:36:03	+52:14:11	0.980	2.50	20.37	...	19.66	22.05	21.01	20.37	0.4425[*]	
PS1J1031+4342	10:31:48	+43:42:57	1.000	2.50	20.19	19.14	18.44	21.62	20.45	19.78	0.39	
PS1J1019+5834	10:19:10	+58:34:49	0.934	2.50	18.11	16.91	16.38	19.92	18.62	18.27	0.2020[*]	
PS1J1007−1021	10:07:14	−10:21:06	0.968	2.50	18.08	17.08	16.55	20.03	18.89	18.44	...	
PS1J0956−0018	09:56:28	−00:18:20	0.965	2.50	20.52	18.92	18.25	22.15	20.59	19.87	0.40	
PS1J0944+3220	09:44:12	+32:20:39	0.960	2.50	...	20.24	19.51	23.2	21.78	20.88	0.5952[*]	
PS1J0913+1819	09:13:39	+18:19:26	1.000	2.50	20.65	19.47	18.94	22.52	21.03	20.27	0.5551[*]	
PS1J0909+3515	09:09:19	+35:15:03	1.000	2.50	...	19.49	18.65	22.71	21.0	20.04	0.4825[*]	
PS1J0410−1453	04:10:31	−14:53:36	0.931	2.50	21.23	20.3	19.47	22.68	21.33	20.44	...	
PS1J0219+2007	02:19:57	+20:07:47	1.000	2.50	20.03	19.92	19.31	21.79	21.06	20.18	0.16	
PS1J0215−2241	02:15:03	−22:41:38	0.940	2.50	20.41	19.11	18.48	22.34	20.64	19.78	...	
PS1J0203−2338	02:03:04	−23:38:03	0.990	2.50	21.3	20.08	18.85	22.66	21.35	20.19	...	(a), (i)
PS1J0145−0455	01:45:04	−04:55:51	1.000	2.50	...	20.02	19.17	23.37	21.76	20.74	0.56	(g), (a), (d)
PS1J2350+3654	23:50:08	+36:54:35	1.000	2.25	20.49	18.75	18.12	21.39	20.12	19.37	0.27	(j)
PS1J2349−0328	23:49:55	−03:28:12	0.951	2.25	20.76	18.94	18.2	21.74	20.19	19.49	0.3453[*]	
PS1J2345−0209	23:45:40	−02:09:41	1.000	2.25	19.78	18.7	17.53	21.17	19.77	19.19	0.2940[*]	
PS1J2327+1341	23:27:57	+13:41:49	0.986	2.25	20.95	19.77	18.56	22.43	21.0	20.12	0.4700[*]	
PS1J2319+1150	23:19:35	+11:50:16	0.993	2.25	...	20.22	19.48	22.95	21.5	20.43	0.5397[*]	
PS1J2315+0158	23:15:55	+01:58:03	1.000	2.25	20.69	19.62	18.82	22.34	20.97	20.21	0.36	
PS1J2309+2820	23:09:26	+28:20:17	0.999	2.25	20.49	19.44	18.81	21.86	20.59	19.84	0.3118[*]	
PS1J2307−1024	23:07:54	−10:24:14	0.957	2.25	19.57	18.89	18.49	21.16	20.25	19.82	0.19	
PS1J2252−0216	22:52:18	−02:16:48	1.000	2.25	19.71	18.9	18.51	21.27	20.19	19.63	0.15	
PS1J2249+3228	22:49:03	+32:28:18	1.000	2.25	18.98	17.75	17.09	19.98	18.64	18.02	0[*]	
PS1J2241−0353	22:41:40	−03:53:00	0.956	2.25	19.29	18.08	17.49	20.57	19.36	18.7	0.20	
PS1J2238+2219	22:38:27	+22:19:13	0.998	2.25	19.98	19.27	19.12	21.4	20.64	20.39	0.33	
PS1J2233+0257	22:33:47	+02:57:55	0.973	2.25	20.49	19.5	18.92	22.04	20.71	20.06	0.22	
PS1J2227+1522	22:27:52	+15:22:58	0.981	2.25	20.56	19.46	19.01	22.42	21.13	20.55	0.39	
PS1J2225+2625	22:25:30	+26:25:54	0.930	2.25	...	19.79	19.39	22.22	20.58	20.08	0.33	
PS1J2204−0635	22:04:56	−06:35:54	0.921	2.25	21.11	19.67	18.6	22.48	21.09	20.09	0.52	
PS1J2159+0049	21:59:33	+00:49:29	1.000	2.25	19.85	19.08	18.65	21.37	20.36	19.78	0.16	
PS1J2143+2251	21:43:45	+22:51:47	0.995	2.25	19.99	19.07	18.59	21.54	20.6	20.09	0.26	
PS1J2140−0149	21:40:52	−01:49:38	0.988	2.25	20.99	20.33	19.35	23.1	21.53	20.56	0.5843[*]	(a)
PS1J2115+1011	21:15:15	+10:11:53	0.962	2.25	...	19.62	18.86	22.78	21.33	20.34	0.53	
PS1J2027−2026	20:27:10	−20:26:01	1.000	2.25	...	18.0	17.62	20.73	19.68	19.14	...	
PS1J1944+6803	19:44:00	+68:03:28	0.924	2.25	20.42	19.0	18.11	21.3	19.77	18.97	...	
PS1J1931+4250	19:31:41	+42:50:26	0.937	2.25	20.75	20.09	19.14	22.36	21.35	20.44	...	
PS1J1640+1932	16:40:46	+19:32:57	1.000	2.25	18.22	16.98	16.37	19.67	18.46	17.89	0.1954[*]	(k)
PS1J1610+0203	16:10:19	+02:03:12	0.962	2.25	19.31	18.23	17.85	20.46	19.41	18.91	...	

Table A.1. Final list of galaxy-scale strong lens candidates with lens LRGs from our systematic search in Pan-STARRS. See Table 1 caption.

Name	RA	Dec	p_{CNN}	Grade	g_{Kron}	r_{Kron}	i_{Kron}	g_{aper}	r_{aper}	i_{aper}	Redshift	Notes
PS1J1609−0805	16:09:26	−08:05:02	0.942	2.25	...	19.35	18.78	22.22	21.09	20.55	...	
PS1J1553+2643	15:53:47	+26:43:38	1.000	2.25	19.92	19.06	18.54	21.49	20.32	19.64	0.36	
PS1J1541+1308	15:41:03	+13:08:11	0.926	2.25	21.59	20.53	19.58	23.27	21.82	20.82	0.6015[*]	
PS1J1530+4454	15:30:18	+44:54:24	0.935	2.25	18.43	17.41	16.97	19.65	18.65	18.18	0.1607[*]	
PS1J1444−0148	14:44:14	−01:48:30	0.992	2.25	21.36	20.41	19.48	22.88	21.54	20.56	0.6333[*]	
PS1J1437+7439	14:37:05	+74:39:01	1.000	2.25	...	...	...	20.96	19.54	18.87	...	
PS1J1425+2134	14:25:32	+21:34:16	0.993	2.25	20.24	18.97	18.45	21.80	20.27	19.62	0.29	
PS1J1414+6447	14:14:15	+64:47:57	0.980	2.25	...	18.39	17.89	21.75	20.09	19.41	0.3598[*]	
PS1J1414+1652	14:14:07	+16:52:09	0.950	2.25	21.72	20.34	19.57	23.14	21.63	20.58	0.6239[*]	
PS1J1412+2052	14:12:10	+20:52:22	1.000	2.25	21.35	20.04	19.35	22.71	21.37	20.51	0.5226[*]	
PS1J1356+1101	13:56:44	+11:01:41	0.950	2.25	19.45	18.35	17.94	21.27	20.09	19.47	0.21	
PS1J1343+1929	13:43:48	+19:29:43	0.993	2.25	19.60	18.14	17.49	21.02	19.59	18.90	0.9308[*]	
PS1J1319−0948	13:19:32	−09:48:19	1.000	2.25	...	...	18.90	20.85	20.30	19.59	...	
PS1J1312+0823	13:12:48	+08:23:37	0.961	2.25	19.03	17.83	17.15	20.22	18.98	18.38	0.2099[*]	
PS1J1233+1407	12:33:20	+14:07:57	0.994	2.25	21.03	20.10	19.33	22.36	21.38	20.43	0.5073[*]	
PS1J1209+2704	12:09:12	+27:04:17	1.000	2.25	20.60	19.02	18.30	21.93	20.20	19.61	0.4426[*]	
PS1J1152−1432	11:52:59	−14:32:14	0.961	2.25	19.48	18.75	18.36	20.96	20.08	19.46	...	
PS1J1135+5124	11:35:56	+51:24:07	0.934	2.25	20.38	19.03	18.35	22.62	20.89	20.17	0.4418[*]	
PS1J1022−0025	10:22:09	−00:25:17	0.966	2.25	20.42	18.58	17.83	21.66	20.09	19.25	0.3940[*]	(f)
PS1J0948+4311	09:48:17	+43:11:36	0.900	2.25	21.40	20.43	19.57	22.95	21.33	20.63	0.37	
PS1J0943+5646	09:43:01	+56:46:22	0.904	2.25	20.32	19.28	18.63	22.08	20.49	19.81	0.3	
PS1J0942+6617	09:42:43	+66:17:36	0.976	2.25	20.45	19.08	18.48	21.99	20.41	19.75	0.26	
PS1J0846−0149	08:46:39	−01:49:43	0.936	2.25	21.07	19.45	18.53	22.29	20.69	19.96	0.45	
PS1J0831+0052	08:31:21	+00:52:57	0.908	2.25	...	...	19.57	23.44	22.00	20.79	0.75	
PS1J0826+0956	08:26:23	+09:56:50	0.986	2.25	...	20.27	19.28	23.34	21.67	20.78	0.4901[*]	
PS1J0755+2738	07:55:02	+27:38:18	1.000	2.25	...	20.00	19.21	22.44	21.44	20.61	0.4079[*]	
PS1J0740+4414	07:40:09	+44:14:10	1.000	2.25	...	...	19.20	22.97	21.57	20.55	0.36	
PS1J0716+3353	07:16:44	+33:53:24	0.942	2.25	...	...	...	22.09	21.44	20.63	...	
PS1J0716+3821	07:16:34	+38:21:07	0.998	2.25	20.40	18.95	18.20	22.14	20.27	19.64	...	
PS1J0654+3616	06:54:21	+36:16:26	0.901	2.25	20.93	19.32	18.65	22.78	21.01	20.07	...	
PS1J0523−3017	05:23:21	−30:17:08	0.978	2.25	20.32	19.19	18.60	21.69	20.60	20.01	...	
PS1J0449−0803	04:49:52	−08:03:37	0.994	2.25	19.96	18.79	18.15	21.69	20.05	19.41	...	
PS1J0435−2520	04:35:37	−25:20:01	0.973	2.25	21.04	19.81	18.73	22.76	21.12	20.14	...	
PS1J0418−2028	04:18:45	−20:28:02	0.992	2.25	19.41	18.55	18.05	21.32	20.37	19.81	...	
PS1J0347−2803	03:47:57	−28:03:11	1.000	2.25	19.52	18.23	17.59	21.17	19.66	18.99	...	
PS1J0254−3050	02:54:18	−30:50:18	1.000	2.25	...	20.59	19.71	22.87	21.86	20.93	...	
PS1J0250−0956	02:50:06	−09:56:08	0.934	2.25	20.90	19.82	19.21	22.54	21.40	20.67	...	
PS1J0246−1249	02:46:31	−12:49:55	1.000	2.25	...	19.99	19.17	23.43	21.54	20.68	...	
PS1J0244−1715	02:44:28	−17:15:03	1.000	2.25	...	18.48	18.10	22.23	20.62	19.92	...	
PS1J0236−1635	02:36:54	−16:35:37	1.000	2.25	18.34	17.81	17.40	20.14	19.34	18.86	0.16	
PS1J0225−1544	02:25:06	−15:44:48	0.907	2.25	19.76	18.80	18.31	21.78	20.76	20.02	...	
PS1J0200−1215	02:00:14	−12:15:53	0.921	2.25	20.73	19.26	18.58	22.71	20.97	20.16	...	
PS1J0159−1608	01:59:06	−16:08:44	1.000	2.25	19.91	18.70	17.71	21.60	20.35	19.37	0.54	
PS1J0146−0600	01:46:28	−06:00:55	0.953	2.25	21.47	20.63	20.04	22.89	21.87	20.88	0.51	
PS1J0118+0318	01:18:09	+03:18:16	0.922	2.25	17.27	16.65	16.23	19.04	18.29	17.93	0.08	
PS1J0111+1059	01:11:27	+10:59:04	0.999	2.25	19.75	18.54	17.96	21.35	20.00	19.29	0.32	
PS1J0101−1341	01:01:55	−13:41:19	0.953	2.25	20.12	18.88	18.34	21.90	20.53	19.92	...	
PS1J0050+1056	00:50:09	+10:56:14	0.994	2.25	21.27	20.24	19.36	22.68	21.61	20.58	0.37	
PS1J0036−0108	00:36:09	−01:08:36	1.000	2.25	19.53	18.76	18.16	21.35	20.26	19.58	0.17	
PS1J0026+0541	00:26:29	+05:41:15	0.912	2.25	21.33	20.13	18.92	22.45	21.10	20.20	0.4560[*]	
PS1J0024−0135	00:24:39	−01:35:20	0.944	2.25	20.54	19.99	19.38	22.23	21.36	20.62	0.33	
PS1J2359+2258	23:59:45	+22:58:09	0.991	2.00	20.86	19.77	19.15	22.50	21.36	20.61	0.24	
PS1J2348+2520	23:48:16	+25:20:11	0.972	2.00	20.35	19.50	19.26	21.65	20.74	20.42	0.41	
PS1J2340−1125	23:40:42	−11:25:28	0.950	2.00	20.40	19.87	...	22.30	21.24	20.69	...	
PS1J2338+2546	23:38:37	+25:46:31	1.000	2.00	20.79	19.34	18.37	22.17	20.46	19.49	0.3802[*]	
PS1J2337+0608	23:37:52	+06:08:42	0.997	2.00	20.62	19.28	18.67	21.81	20.51	19.76	0.32	
PS1J2337−0425	23:37:01	−04:25:25	1.000	2.00	20.20	19.15	18.56	21.68	20.34	19.71	0.22	
PS1J2336+0445	23:36:57	+04:45:59	0.932	2.00	18.34	17.14	16.72	20.24	19.14	18.52	0.26	
PS1J2318−1404	23:18:53	−14:04:58	0.993	2.00	20.48	19.19	18.55	21.94	20.34	19.57	...	
PS1J2259−1322	22:59:34	−13:22:49	0.912	2.00	20.70	19.89	19.29	22.20	21.07	20.20	...	
PS1J2251−1738	22:51:10	−17:38:27	0.971	2.00	21.08	19.49	18.57	22.43	20.61	19.79	0.53	
PS1J2247−0644	22:47:54	−06:44:47	0.935	2.00	20.06	19.05	18.58	21.55	20.27	19.58	0.30	
PS1J2239−1142	22:39:28	−11:42:06	0.928	2.00	19.25	17.71	18.12	21.16	19.70	19.13	...	
PS1J2225−1236	22:25:33	−12:36:21	0.934	2.00	20.26	...	18.81	21.84	20.46	19.91	...	
PS1J2219−0617	22:19:10	−06:17:22	1.000	2.00	21.54	19.82	18.83	22.51	20.86	19.95	0.39	

Table A.2. continued.

Name	RA	Dec	p_{CNN}	Grade	g_{Kron}	r_{Kron}	i_{Kron}	g_{aper}	r_{aper}	i_{aper}	Redshift	Notes
PS1J2215−0214	22:15:46	−02:14:04	0.918	2.00	20.85	19.04	18.30	22.03	20.23	19.52	0.3746[(*)]	
PS1J2213−2854	22:13:23	−28:54:48	0.999	2.00	20.37	19.30	18.48	22.00	20.43	19.74	...	
PS1J2208+1712	22:08:25	+17:12:39	0.930	2.00	20.85	19.65	18.92	22.26	20.82	20.11	0.4682[(*)]	
PS1J2157−0836	21:57:57	−08:36:05	1.000	2.00	...	...	...	22.08	20.95	20.13	0.34	
PS1J2156+2329	21:56:03	+23:29:43	1.000	2.00	18.66	17.62	17.12	19.85	18.83	18.37	0.17	
PS1J2155−0650	21:55:12	−06:50:34	1.000	2.00	20.77	19.98	19.26	22.68	21.32	20.50	0.53	
PS1J2154−0248	21:54:32	−02:48:19	0.940	2.00	20.37	18.63	17.79	21.63	19.90	19.32	0.3589[(*)]	
PS1J2128+2517	21:28:50	+25:17:39	0.955	2.00	20.78	19.34	18.84	22.07	20.67	20.02	0.35	
PS1J2122−0431	21:22:00	−04:31:15	1.000	2.00	20.20	19.35	18.96	21.82	20.57	19.97	0.46	
PS1J2121+2030	21:21:56	+20:30:41	0.980	2.00	...	19.66	18.82	23.18	21.20	20.30	0.50	
PS1J2104+0407	21:04:15	+04:07:41	0.999	2.00	21.00	19.10	18.43	22.24	20.50	19.82	0.37	
PS1J2101+0616	21:01:39	+06:16:22	0.951	2.00	19.83	19.72	19.13	21.77	21.09	20.30	0.23	
PS1J2044−1218	20:44:26	−12:18:39	0.965	2.00	20.60	19.46	18.89	22.00	20.49	20.01	...	
PS1J1832+6936	18:32:29	+69:36:08	0.935	2.00	20.59	18.82	18.24	21.80	20.16	19.54	...	
PS1J1817+5830	18:17:29	+58:30:52	0.951	2.00	20.57	19.25	18.59	21.88	20.52	19.78	...	
PS1J1809+6036	18:09:10	+60:36:53	0.963	2.00	19.92	19.17	18.67	21.32	20.47	19.91	...	
PS1J1805+2430	18:05:26	+24:30:08	1.000	2.00	20.31	18.77	18.12	21.73	20.30	19.70	0.25	
PS1J1758+6342	17:58:06	+63:42:40	0.994	2.00	21.32	19.84	18.99	22.49	21.13	20.27	0.50	
PS1J1757+3631	17:57:44	+36:31:24	1.000	2.00	18.43	17.59	17.15	20.02	18.90	18.41	...	
PS1J1748+3358	17:48:30	+33:58:10	1.000	2.00	20.89	20.00	19.30	22.29	21.20	20.41	...	
PS1J1741+5658	17:41:26	+56:58:20	0.952	2.00	21.60	20.55	19.61	23.25	21.94	20.94	0.55	
PS1J1730+3405	17:30:15	+34:05:08	0.990	2.00	20.75	19.06	18.35	22.00	20.28	19.68	0.4219[(*)]	
PS1J1724+3146	17:24:12	+31:46:35	1.000	2.00	18.44	17.26	16.80	19.90	18.72	18.24	0.2097[(*)]	
PS1J1713+2719	17:13:14	+27:19:52	0.937	2.00	18.25	17.32	16.92	19.74	18.69	18.30	0.14	
PS1J1705+2849	17:05:55	+28:49:59	0.990	2.00	21.50	19.62	18.84	22.73	20.90	20.11	0.4680[(*)]	
PS1J1657+2341	16:57:48	+23:41:09	0.947	2.00	19.44	18.10	17.53	20.73	19.40	18.89	0.25	
PS1J1657+2746	16:57:48	+27:46:09	0.939	2.00	19.55	18.06	17.46	20.80	19.33	18.78	0.27	
PS1J1649+3049	16:49:40	+30:49:09	0.921	2.00	20.63	19.21	18.57	22.01	20.32	19.68	0.4096[(*)]	
PS1J1643+3927	16:43:31	+39:27:44	0.925	2.00	22.04	20.24	19.16	22.83	21.37	20.47	0.5134[(*)]	
PS1J1634+1119	16:34:38	+11:19:13	1.000	2.00	19.81	18.75	18.25	21.29	20.12	19.63	0.19	
PS1J1631+0013	16:31:37	+00:13:53	0.959	2.00	20.27	18.84	18.23	21.24	19.80	19.15	0.30	
PS1J1625+2224	16:25:05	+22:24:41	0.981	2.00	21.03	19.79	19.24	22.40	21.16	20.48	0.36	
PS1J1620+5626	16:20:12	+56:26:18	0.970	2.00	21.63	20.12	19.18	22.91	21.20	20.36	0.48	
PS1J1615+4811	16:15:41	+48:11:07	0.977	2.00	19.69	18.43	17.85	21.25	20.10	19.56	0.21	
PS1J1613+0146	16:13:10	+01:46:18	0.963	2.00	21.22	19.88	18.98	22.65	21.14	20.27	...	
PS1J1605+1306	16:05:23	+13:06:17	0.968	2.00	20.41	18.99	18.14	21.94	20.25	19.52	0.3971[(*)]	
PS1J1603+0310	16:03:07	+03:10:44	1.000	2.00	20.42	19.46	18.97	21.97	20.85	20.13	0.20	
PS1J1558+2429	15:58:37	+24:29:04	0.974	2.00	21.07	19.03	18.25	22.59	20.80	19.93	0.4268[(*)]	
PS1J1552+4806	15:52:56	+48:06:26	0.998	2.00	22.49	20.57	19.59	23.50	21.68	20.73	0.6228[(*)]	
PS1J1551+2156	15:51:59	+21:56:04	1.000	2.00	15.98	15.34	15.07	18.16	17.35	17.04	0.0258[(*)]	
PS1J1548+2156	15:48:53	+21:56:16	0.956	2.00	20.04	19.10	18.65	21.94	20.77	20.19	0.31	
PS1J1547+0047	15:47:59	+00:47:37	0.918	2.00	19.22	18.05	17.50	20.49	19.25	18.65	0.18	
PS1J1545−1807	15:45:08	−18:07:12	0.999	2.00	...	20.04	19.34	22.80	21.32	20.41	...	
PS1J1541+6809	15:41:47	+68:09:14	0.982	2.00	...	19.36	18.47	22.19	20.69	19.75	...	
PS1J1539+1425	15:39:44	+14:25:51	0.999	2.00	20.71	19.48	18.84	22.14	20.79	20.14	0.25	
PS1J1539+1706	15:39:35	+17:06:47	0.961	2.00	19.77	18.53	17.92	21.26	19.91	19.32	0.28018[(*)]	
PS1J1534+0622	15:34:28	+06:22:16	1.000	2.00	20.27	19.27	18.77	21.86	20.63	19.98	0.27	
PS1J1510−2039	15:10:00	−20:39:28	0.979	2.00	...	...	19.83	22.94	21.72	20.76	...	
PS1J1501−0330	15:01:20	−03:30:13	0.981	2.00	20.67	19.62	18.80	22.39	20.75	19.97	...	
PS1J1453−2246	14:53:59	−22:46:07	0.993	2.00	...	20.11	19.18	23.01	21.15	20.25	...	
PS1J1452+1047	14:52:28	+10:47:37	1.000	2.00	18.86	17.81	17.33	20.45	19.31	18.78	0.2863[(*)]	
PS1J1438+4907	14:38:03	+49:07:33	0.966	2.00	21.59	20.31	19.23	22.86	21.52	20.32	0.5932[(*)]	
PS1J1436−0223	14:36:41	−02:23:15	0.966	2.00	20.29	19.50	19.09	22.14	20.71	20.18	0.35	
PS1J1433+0300	14:33:55	+03:00:14	0.919	2.00	21.43	20.32	19.48	22.89	21.63	20.65	0.59	(f)
PS1J1430−2524	14:30:40	−25:24:41	0.931	2.00	...	...	18.63	21.76	20.71	19.73	...	
PS1J1412−0712	14:12:16	−07:12:49	0.988	2.00	21.37	20.35	19.49	22.91	21.61	20.56	...	
PS1J1412+0432	14:12:07	+04:32:26	0.905	2.00	21.77	20.31	19.52	23.21	21.69	20.76	0.5940[(*)]	
PS1J1404+4455	14:04:30	+44:55:14	0.968	2.00	19.19	17.99	17.48	20.49	19.27	18.75	0.2187[(*)]	
PS1J1403−0208	14:03:53	−02:08:19	0.946	2.00	21.14	19.90	19.17	22.74	20.96	20.15	0.41	
PS1J1355+0011	13:55:12	+00:11:09	0.998	2.00	21.13	19.81	...	22.28	20.82	20.18	0.29	
PS1J1351−0623	13:51:20	−06:23:00	0.944	2.00	...	19.94	18.69	23.03	21.50	20.37	0.56	
PS1J1349−0817	13:49:31	−08:17:56	0.987	2.00	20.55	19.27	18.62	22.28	20.65	20.23	...	
PS1J1341−0247	13:41:22	−02:47:41	0.929	2.00	20.62	19.45	18.78	21.95	20.52	19.84	0.39	
PS1J1340−0503	13:40:45	−05:03:11	0.938	2.00	20.12	19.47	19.16	21.81	20.82	20.37	...	
PS1J1336+3328	13:36:46	+33:28:40	1.000	2.00	18.85	17.61	17.07	20.55	19.31	18.65	0.23	

Table A.3. continued.

Name	RA	Dec	p_{CNN}	Grade	g_{Kron}	r_{Kron}	i_{Kron}	g_{aper}	r_{aper}	i_{aper}	Redshift	Notes
PS1J1327+2926	13:27:54	+29:26:53	0.971	2.00	20.81	19.65	18.93	22.12	20.93	19.95	0.25	
PS1J1326−0324	13:26:55	−03:24:21	0.970	2.00	21.25	20.01	19.28	22.65	21.01	20.25	0.4823[*]	
PS1J1316+2859	13:16:44	+28:59:05	0.978	2.00	20.29	18.99	18.38	21.60	20.30	19.60	0.32	
PS1J1315+0104	13:15:34	+01:04:52	0.936	2.00	21.75	19.72	18.74	23.20	21.59	20.61	0.52	
PS1J1309+0757	13:09:38	+07:57:36	0.982	2.00	18.93	17.85	17.38	20.67	19.42	18.91	0.2129[*]	
PS1J1304+2302	13:04:46	+23:02:06	0.981	2.00	20.85	19.87	19.32	22.20	20.97	20.30	0.5891[*]	
PS1J1301+4123	13:01:43	+41:23:29	0.986	2.00	19.75	18.46	17.88	20.91	19.55	18.97	0.2806[*]	
PS1J1259−0455	12:59:38	−04:55:28	0.906	2.00	20.10	18.63	17.92	21.68	20.13	19.61	...	
PS1J1253−0415	12:53:09	−04:15:43	1.000	2.00	21.15	19.45	18.79	22.19	20.62	19.96	...	
PS1J1244+1802	12:44:35	+18:02:11	0.992	2.00	20.69	20.10	19.39	22.43	21.02	20.30	0.34	
PS1J1242+0855	12:42:34	+08:55:34	0.981	2.00	21.02	19.41	18.70	22.19	20.62	19.84	0.4648[*]	
PS1J1237+2623	12:37:57	+26:23:04	0.908	2.00	20.67	20.64	19.73	22.80	21.41	20.85	0.62	
PS1J1221+1406	12:21:55	+14:06:15	0.977	2.00	20.02	18.82	18.13	21.95	20.43	19.61	0.4199[*]	
PS1J1215+1847	12:15:57	+18:47:24	0.964	2.00	20.05	18.78	18.19	21.47	19.79	19.21	0.3569[*]	
PS1J1211+4200	12:11:40	+42:00:20	0.937	2.00	20.55	19.33	18.73	22.01	20.60	19.86	0.27	
PS1J1206+5302	12:06:24	+53:02:38	0.999	2.00	20.70	20.02	19.33	22.66	21.15	20.45	0.37	
PS1J1157−1828	11:57:27	−18:28:37	0.957	2.00	...	19.80	19.05	22.69	20.93	20.28	...	
PS1J1156+5032	11:56:48	+50:32:32	0.987	2.00	...	20.19	19.26	22.71	21.41	20.34	0.5889[*]	
PS1J1149+6054	11:49:06	+60:54:27	0.991	2.00	20.06	19.19	18.85	21.73	20.63	20.14	0.18	
PS1J1148+1347	11:48:07	+13:47:30	0.956	2.00	20.07	18.37	17.64	21.22	19.77	19.06	0.3052[*]	
PS1J1147+2609	11:47:43	+26:09:52	0.992	2.00	...	20.40	19.28	22.72	21.43	20.35	0.5486[*]	
PS1J1142+5830	11:42:27	+58:30:45	0.995	2.00	19.75	18.38	17.74	21.50	19.88	19.30	0.30	
PS1J1139+5252	11:39:57	+52:52:58	0.990	2.00	21.61	19.80	18.85	23.05	21.38	20.38	0.5378[*]	
PS1J1136+1633	11:36:41	+16:33:56	0.973	2.00	20.27	...	...	22.01	20.75	20.15	0.4236[*]	
PS1J1134+1712	11:34:28	+17:12:29	0.970	2.00	19.93	18.77	18.12	21.32	20.06	19.40	0.3752[*]	
PS1J1132+5436	11:32:40	+54:36:26	1.000	2.00	20.22	19.43	18.98	22.02	20.77	20.23	0.25	
PS1J1120−0851	11:20:00	−08:51:00	0.996	2.00	...	20.21	19.14	23.53	21.80	20.70	0.54	
PS1J1117+7111	11:17:50	+71:11:22	1.000	2.00	18.94	17.70	17.09	20.45	19.06	18.63	...	
PS1J1108−0143	11:08:18	−01:43:02	0.980	2.00	21.27	19.81	18.87	22.77	21.38	20.49	0.4707[*]	
PS1J1106+1635	11:06:04	+16:35:16	1.000	2.00	20.19	18.61	18.00	21.53	19.91	19.28	0.3631[*]	
PS1J1105+5503	11:05:02	+55:03:09	0.948	2.00	20.66	19.82	18.98	21.78	20.70	20.02	0.4625[*]	
PS1J1104+4118	11:04:22	+41:18:41	1.000	2.00	19.66	18.30	17.90	20.99	19.59	19.13	0.28	
PS1J1104−0654	11:04:21	−06:54:04	1.000	2.00	...	19.82	19.24	22.95	21.51	20.95	...	
PS1J1104−0409	11:04:05	−04:09:09	0.992	2.00	19.24	18.64	18.39	20.84	20.19	19.85	...	
PS1J1101+1822	11:01:16	+18:22:54	0.995	2.00	20.25	19.53	19.34	21.77	21.05	20.72	0.36	
PS1J1040+3029	10:40:52	+30:29:12	0.998	2.00	20.31	19.75	19.24	21.95	20.88	20.19	0.4374[*]	
PS1J1033+2316	10:33:10	+23:16:20	0.972	2.00	20.26	18.85	18.06	21.16	19.87	19.14	0.30	
PS1J1028+3820	10:28:11	+38:20:24	0.987	2.00	20.83	...	19.59	22.15	21.51	20.45	0.35	
PS1J1014+3504	10:14:25	+35:04:48	1.000	2.00	20.10	18.67	17.94	21.54	20.08	19.42	0.36	
PS1J1013+1011	10:13:04	+10:11:34	0.912	2.00	21.49	20.02	19.23	22.88	21.44	20.50	0.5161[*]	
PS1J1001+2133	10:01:25	+21:33:57	0.999	2.00	19.42	18.82	18.54	21.20	20.36	19.98	0.27	
PS1J0948−0233	09:48:38	−02:33:34	0.921	2.00	20.71	20.15	19.31	21.98	21.43	20.60	0.6111[*]	
PS1J0934−0007	09:34:54	−00:07:26	0.958	2.00	...	19.30	18.92	22.01	20.56	20.02	0.31	
PS1J0933−0247	09:33:59	−02:47:18	0.991	2.00	20.39	19.75	19.01	22.00	21.02	20.13	0.43	
PS1J0931+2601	09:31:50	+26:01:35	0.966	2.00	...	...	18.57	21.25	20.12	19.68	0.3248[*]	
PS1J0931+4010	09:31:09	+40:10:16	0.995	2.00	20.42	19.49	18.95	21.80	20.57	19.96	0.46	
PS1J0923+1259	09:23:14	+12:59:40	0.993	2.00	19.91	18.96	18.44	21.35	20.28	19.45	0.21	
PS1J0919+1707	09:19:58	+17:07:11	0.931	2.00	20.22	19.00	18.66	22.32	20.74	20.28	0.28	
PS1J0917+3109	09:17:27	+31:09:25	0.994	2.00	19.05	17.81	17.30	20.71	19.50	18.88	0.2386[*]	
PS1J0911−0633	09:11:46	−06:33:03	0.998	2.00	19.90	18.49	17.89	21.16	19.82	19.09	...	
PS1J0909+4827	09:09:51	+48:27:27	1.000	2.00	20.83	19.61	19.15	22.47	21.35	20.88	0.35	
PS1J0909+2329	09:09:11	+23:29:45	1.000	2.00	20.72	19.85	19.10	22.25	20.96	20.33	0.33	
PS1J0907+7720	09:07:14	+77:20:47	0.951	2.00	21.16	19.93	19.00	22.33	21.17	20.43	...	
PS1J0858+0946	08:58:46	+09:46:58	0.951	2.00	20.96	19.62	18.69	22.40	20.78	19.99	0.4543[*]	
PS1J0857+0655	08:57:10	+06:55:25	0.999	2.00	20.64	19.64	18.95	22.15	21.08	20.41	0.46	
PS1J0857+2633	08:57:09	+26:33:30	0.933	2.00	20.59	19.42	18.74	22.57	21.15	20.37	0.36	
PS1J0838+2218	08:38:18	+22:18:02	0.968	2.00	20.81	20.06	19.06	22.62	21.00	20.15	0.5242[*]	
PS1J0834+1443	08:34:50	+14:43:49	0.934	2.00	19.44	18.19	17.75	20.79	19.49	18.97	0.2558[*]	
PS1J0831+4121	08:31:25	+41:21:09	0.919	2.00	21.57	20.07	18.95	22.93	21.22	20.26	0.4869[*]	
PS1J0821−0833	08:21:12	−08:33:46	1.000	2.00	20.22	19.15	18.65	21.79	20.39	19.76	...	
PS1J0819−0911	08:19:13	−09:11:02	0.981	2.00	20.85	18.94	18.38	22.21	20.31	19.68	...	
PS1J0815+6512	08:15:38	+65:12:45	0.901	2.00	21.32	20.29	19.48	23.19	21.91	20.76	0.62	
PS1J0746+1255	07:46:34	+12:55:53	0.998	2.00	...	19.77	18.96	22.70	20.97	20.16	0.46	
PS1J0730+5237	07:30:56	+52:37:27	0.906	2.00	21.33	20.00	19.28	22.72	21.17	20.45	...	
PS1J0719+4107	07:19:44	+41:07:03	0.948	2.00	19.55	18.66	18.09	20.92	19.71	19.18	0.20	

Table A.4. continued.

Name	RA	Dec	p_{CNN}	Grade	g_{Kron}	r_{Kron}	i_{Kron}	g_{aper}	r_{aper}	i_{aper}	Redshift	Notes
PS1J0718+3008	07:18:54	+30:08:30	0.993	2.00	20.95	19.11	18.43	22.56	20.75	20.01	0.30	
PS1J0716+6359	07:16:49	+63:59:23	0.979	2.00	21.57	20.37	19.41	23.23	22.09	20.99	...	
PS1J0716+2728	07:16:02	+27:28:52	0.995	2.00	21.19	19.71	18.91	22.91	21.24	20.33	...	
PS1J0708+5002	07:08:47	+50:02:41	0.951	2.00	21.53	19.98	18.99	22.64	21.25	20.38	...	
PS1J0524−0718	05:24:31	−07:18:09	0.945	2.00	19.34	18.08	17.47	20.75	19.48	18.80	...	
PS1J0458−2910	04:58:56	−29:10:07	0.972	2.00	...	20.36	19.66	23.16	21.69	21.03	...	
PS1J0456−2946	04:56:40	−29:46:22	0.920	2.00	20.56	19.32	18.76	22.03	20.91	20.16	...	(a)
PS1J0441+0226	04:41:27	+02:26:50	1.000	2.00	20.71	19.53	18.78	22.33	20.88	20.14	...	
PS1J0432−0237	04:32:53	−02:37:43	0.957	2.00	21.10	20.03	19.16	22.65	21.36	20.21	...	
PS1J0432−0925	04:32:01	−09:25:18	1.000	2.00	20.07	19.36	18.91	21.29	20.45	19.95	...	
PS1J0426−1430	04:26:33	−14:30:48	0.942	2.00	20.96	19.24	18.36	22.66	21.05	19.95	...	
PS1J0417−2910	04:17:48	−29:10:40	1.000	2.00	20.53	18.89	18.18	21.91	20.31	19.61	...	
PS1J0408−0646	04:08:31	−06:46:12	0.948	2.00	20.13	19.33	19.05	21.48	20.61	20.15	...	
PS1J0404−0858	04:04:51	−08:58:03	0.997	2.00	19.45	18.11	17.60	21.13	19.83	19.12	...	
PS1J0359−1453	03:59:45	−14:53:58	1.000	2.00	20.97	19.56	18.73	22.52	21.14	20.13	...	
PS1J0358−0436	03:58:35	−04:36:07	0.916	2.00	19.95	19.31	18.82	22.05	21.16	20.59	0.19	
PS1J0350−2018	03:50:20	−20:18:33	0.966	2.00	20.97	19.68	18.95	22.38	20.78	19.95	...	
PS1J0349−1544	03:49:52	−15:44:22	0.918	2.00	20.44	19.33	18.85	22.49	21.05	20.30	...	
PS1J0329−0344	03:29:42	−03:44:10	0.963	2.00	20.00	19.16	18.64	21.46	20.48	19.92	...	
PS1J0328−1013	03:28:10	−10:13:47	0.925	2.00	21.14	19.76	19.10	22.30	20.85	20.04	...	
PS1J0325−0159	03:25:53	−01:59:31	0.966	2.00	21.03	20.46	19.69	22.63	21.69	21.01	...	
PS1J0317−1513	03:17:28	−15:13:12	0.937	2.00	20.19	19.17	18.76	21.58	20.41	19.80	...	
PS1J0256+0041	02:56:49	+00:41:22	0.963	2.00	20.35	19.62	19.11	21.80	20.99	20.42	0.16	
PS1J0256−2847	02:56:23	−28:47:05	0.959	2.00	21.96	20.14	19.23	23.25	21.30	20.44	...	
PS1J0249+1936	02:49:53	+19:36:04	1.000	2.00	21.21	19.97	18.98	22.95	21.31	20.36	0.48	
PS1J0247+1757	02:47:10	+17:57:31	0.982	2.00	19.15	18.55	18.19	20.84	19.97	19.47	...	
PS1J0242−2755	02:42:03	−27:55:40	0.957	2.00	20.62	19.67	18.64	21.92	20.88	19.89	...	
PS1J0238−2520	02:38:57	−25:20:39	0.901	2.00	20.78	19.88	19.27	22.29	21.39	20.77	...	
PS1J0232−2711	02:32:45	−27:11:51	0.911	2.00	21.02	20.52	19.48	23.19	21.75	20.86	...	
PS1J0229−0619	02:29:04	−06:19:38	1.000	2.00	18.53	17.36	16.86	20.06	19.00	18.35	0.1895$^{(*)}$	
PS1J0227−1014	02:27:47	−10:14:36	0.916	2.00	19.98	18.97	18.54	21.72	20.40	19.86	...	
PS1J0227−2350	02:27:22	−23:50:24	0.905	2.00	...	19.63	19.01	22.81	21.49	20.65	...	
PS1J0215+0231	02:15:38	+02:31:34	0.922	2.00	20.22	19.20	18.64	22.02	20.79	20.10	0.40	
PS1J0214+1932	02:14:52	+19:32:28	0.906	2.00	21.37	20.09	19.08	23.40	21.54	20.31	0.64	
PS1J0214−0206	02:14:08	−02:06:28	0.926	2.00	...	19.97	19.14	23.80	22.01	20.72	0.61	(a), (l)
PS1J0154+0325	01:54:07	+03:25:03	1.000	2.00	20.61	19.64	19.12	22.48	20.99	20.40	0.31	
PS1J0150+0323	01:50:23	+03:23:53	0.907	2.00	21.14	20.42	19.70	22.59	21.76	20.93	0.51	
PS1J0148−1915	01:48:12	−19:15:55	0.999	2.00	20.55	19.16	18.60	21.91	20.29	19.74	...	
PS1J0141−2256	01:41:29	−22:56:43	0.908	2.00	21.43	20.45	19.42	22.62	21.24	20.13	...	
PS1J0138+0247	01:38:58	+02:47:23	0.936	2.00	20.91	19.69	18.91	22.79	21.08	20.33	0.37	
PS1J0137−1620	01:37:45	−16:20:17	0.933	2.00	21.10	20.05	19.30	22.88	21.42	20.54	...	
PS1J0136−1759	01:36:36	−17:59:05	0.954	2.00	20.66	20.65	19.74	22.94	21.82	20.85	0.56	
PS1J0115−3015	01:15:38	−30:15:49	0.919	2.00	21.35	20.66	19.68	23.03	21.70	20.83	...	
PS1J0114−1012	01:14:23	−10:12:06	0.927	2.00	20.83	19.92	19.27	22.27	21.22	20.44	0.38	
PS1J0110−0809	01:10:50	−08:09:45	0.968	2.00	20.74	19.61	19.10	22.33	21.07	20.42	0.27	
PS1J0108−1418	01:08:17	−14:18:26	0.996	2.00	21.46	20.31	19.65	22.64	21.64	20.70	...	
PS1J0100+2346	01:00:36	+23:46:13	0.954	2.00	19.70	18.27	17.70	21.05	19.62	18.95	0.2980$^{(*)}$	
PS1J0100−1311	01:00:02	−13:11:37	0.927	2.00	20.95	20.17	19.36	22.43	21.72	20.95	...	
PS1J0046−1840	00:46:48	−18:40:55	0.954	2.00	20.21	19.49	19.16	21.70	20.95	20.59	...	
PS1J0045−1609	00:45:43	−16:09:49	0.988	2.00	20.46	18.88	18.23	21.86	20.19	19.58	...	
PS1J0045+1006	00:45:30	+10:06:55	1.000	2.00	18.22	17.02	16.44	20.26	18.93	18.30	0.1940$^{(*)}$	
PS1J0044−2405	00:44:18	−24:05:00	0.943	2.00	21.20	20.07	19.22	22.61	21.33	20.56	...	
PS1J0042−1713	00:42:32	−17:13:45	0.911	2.00	20.88	19.73	19.10	22.34	21.03	20.26	...	
PS1J0033+3938	00:33:23	+39:38:59	0.920	2.00	20.52	19.22	18.64	21.86	20.33	19.69	0.32	
PS1J0027+1510	00:27:45	+15:10:02	0.919	2.00	20.77	19.89	19.35	22.98	21.55	20.84	0.33	
PS1J0017+1048	00:17:23	+10:48:53	0.922	2.00	20.84	19.55	18.93	22.25	20.72	20.03	0.31	
PS1J0016−0634	00:16:54	−06:34:01	0.903	2.00	20.30	19.13	18.62	21.90	20.75	20.19	0.28	
PS1J0014+0157	00:14:01	+01:57:51	1.000	2.00	21.44	19.84	19.03	22.66	21.02	20.23	0.38	

Table A.5. continued.
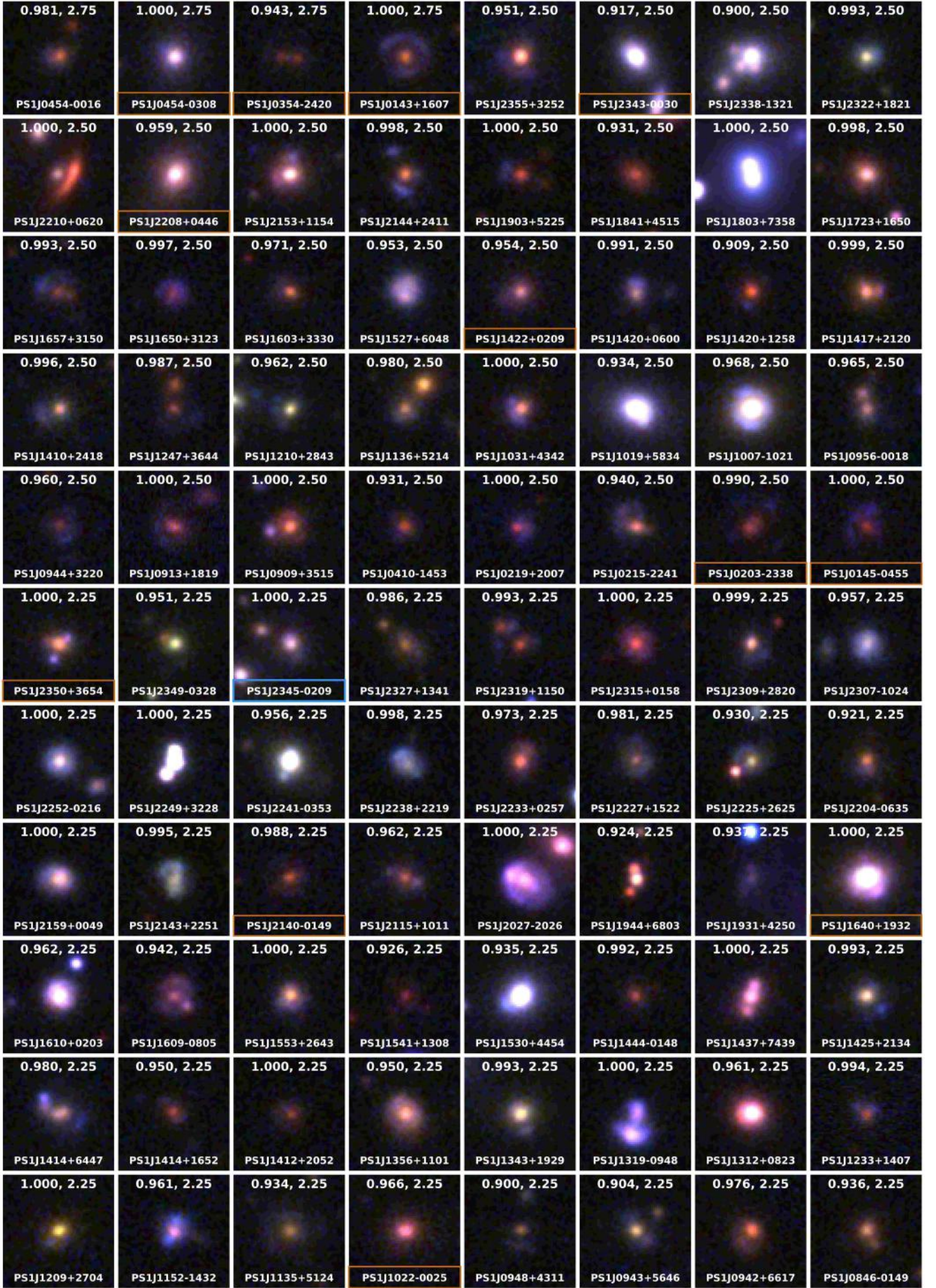
Fig. A.1. Pan-STARRS 3-color *gri* images of candidates with grades ≥ 2 from visual inspection of CNN scores $p_{\text{CNN}} > 0.9$. See Fig. 9 caption.
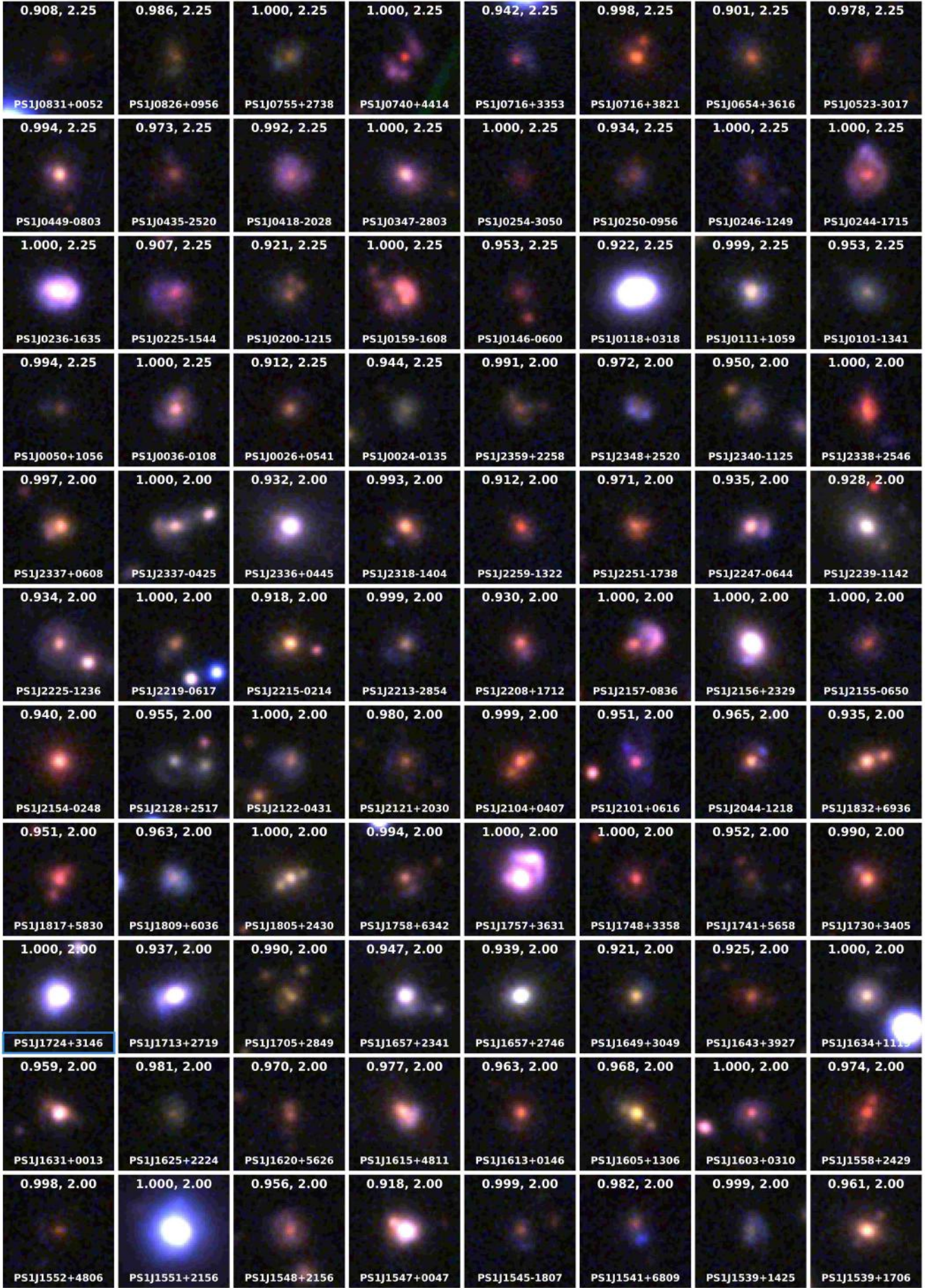
Fig. A.2. continued.
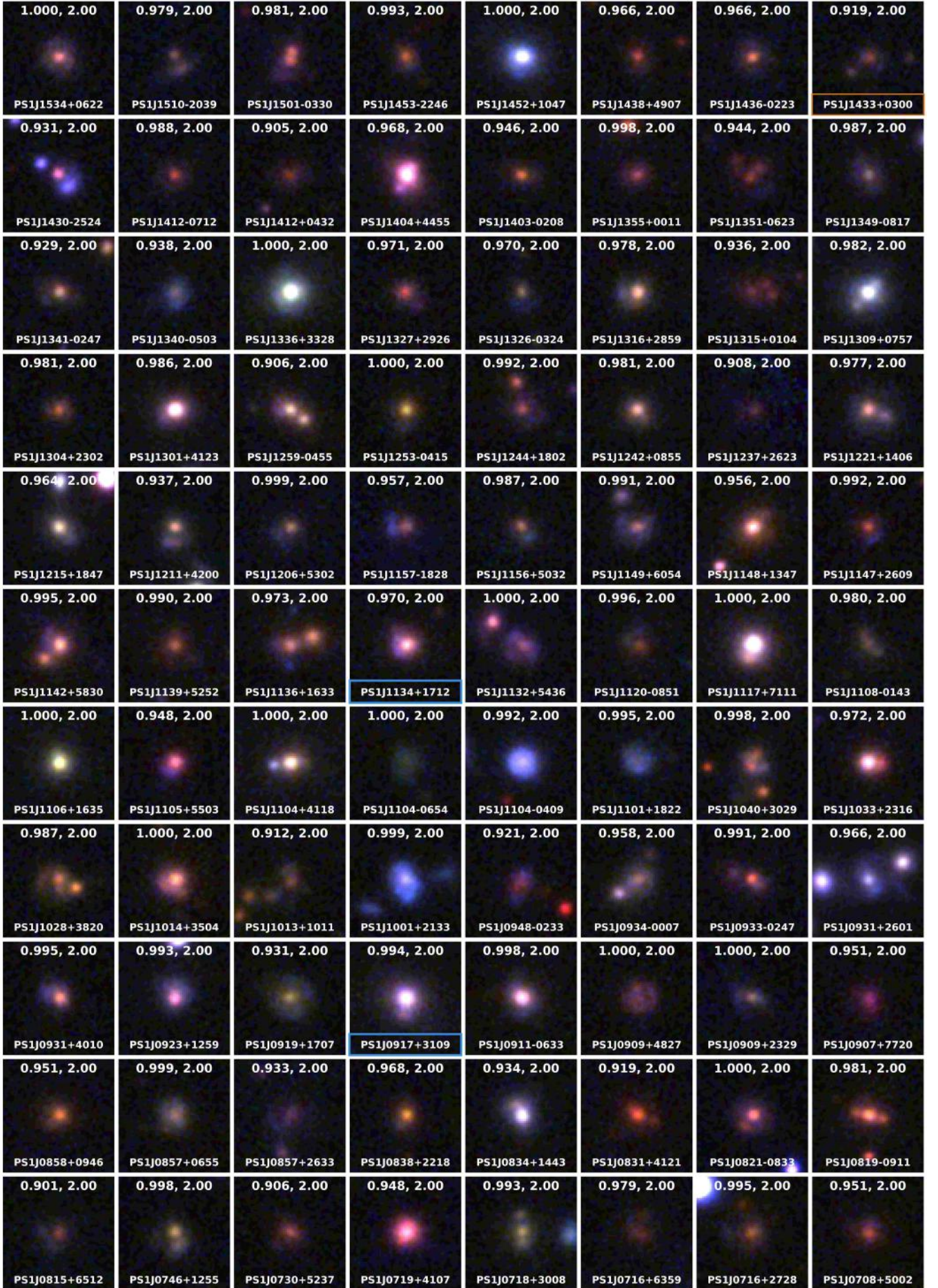
Fig. A.3. continued.

Fig. A.4. continued.

[4] Technical University of Munich, Department of Informatics, Boltzmann-Str. 3, 85748 Garching, Germany

[5] Institute of Physics, Laboratory of Astrophysics, Ecole Polytechnique Fédérale de Lausanne (EPFL), Observatoire de Sauverny, 1290 Versoix, Switzerland

Fig. A.5. Legacy 3-color images of candidates covered in DR8.

0.973, 2.25	0.981, 2.25	0.930, 2.25	0.921, 2.25	1.000, 2.25	0.995, 2.25	0.988, 2.25	0.962, 2.25
PS1J2233+0257	PS1J2227+1522	PS1J2225+2625	PS1J2204-0635	PS1J2159+0049	PS1J2143+2251	PS1J2140-0149	PS1J2115+1011
0.924, 2.25	1.000, 2.25	0.962, 2.25	1.000, 2.25	0.926, 2.25	0.935, 2.25	0.992, 2.25	1.000, 2.25
PS1J1944+6803	PS1J1640+1932	PS1J1610+0203	PS1J1553+2643	PS1J1541+1308	PS1J1530+4454	PS1J1444-0148	PS1J1437+7439
0.993, 2.25	0.980, 2.25	0.950, 2.25	1.000, 2.25	0.950, 2.25	0.993, 2.25	1.000, 2.25	0.961, 2.25
PS1J1425+2134	PS1J1414+6447	PS1J1414+1652	PS1J1412+2052	PS1J1356+1101	PS1J1343+1929	PS1J1319-0948	PS1J1312+0823
0.994, 2.25	1.000, 2.25	0.934, 2.25	0.966, 2.25	0.900, 2.25	0.904, 2.25	0.976, 2.25	0.936, 2.25
PS1J1233+1407	PS1J1209+2704	PS1J1135+5124	PS1J1022-0025	PS1J0948+4311	PS1J0943+5646	PS1J0942+6617	PS1J0846-0149
0.908, 2.25	0.986, 2.25	1.000, 2.25	1.000, 2.25	0.942, 2.25	0.998, 2.25	0.901, 2.25	0.978, 2.25
PS1J0831+0052	PS1J0826+0956	PS1J0755+2738	PS1J0740+4414	PS1J0716+3353	PS1J0716+3821	PS1J0654+3616	PS1J0523-3017
0.994, 2.25	0.973, 2.25	0.992, 2.25	1.000, 2.25	1.000, 2.25	0.934, 2.25	1.000, 2.25	1.000, 2.25
PS1J0449-0803	PS1J0435-2520	PS1J0418-2028	PS1J0347-2803	PS1J0254-3050	PS1J0250-0956	PS1J0246-1249	PS1J0244-1715
1.000, 2.25	0.907, 2.25	0.921, 2.25	1.000, 2.25	0.953, 2.25	0.922, 2.25	0.999, 2.25	0.953, 2.25
PS1J0236-1635	PS1J0225-1544	PS1J0200-1215	PS1J0159-1608	PS1J0146-0600	PS1J0118+0318	PS1J0111+1059	PS1J0101-1341
0.994, 2.25	1.000, 2.25	0.912, 2.25	0.944, 2.25	0.991, 2.00	0.972, 2.00	0.950, 2.00	1.000, 2.00
PS1J0050+1056	PS1J0036-0108	PS1J0026+0541	PS1J0024-0135	PS1J2359+2258	PS1J2348+2520	PS1J2340-1125	PS1J2338+2546
0.997, 2.00	1.000, 2.00	0.932, 2.00	0.993, 2.00	0.912, 2.00	0.935, 2.00	0.928, 2.00	0.934, 2.00
PS1J2337+0608	PS1J2337-0425	PS1J2336+0445	PS1J2318-1404	PS1J2259-1322	PS1J2247-0644	PS1J2239-1142	PS1J2225-1236
1.000, 2.00	0.918, 2.00	0.930, 2.00	1.000, 2.00	1.000, 2.00	1.000, 2.00	0.940, 2.00	0.955, 2.00
PS1J2219-0617	PS1J2215-0214	PS1J2208+1712	PS1J2157-0836	PS1J2156+2329	PS1J2155-0650	PS1J2154-0248	PS1J2128+2517
1.000, 2.00	0.980, 2.00	0.999, 2.00	0.951, 2.00	0.935, 2.00	0.951, 2.00	0.963, 2.00	1.000, 2.00
PS1J2122-0431	PS1J2121+2030	PS1J2104+0407	PS1J2101+0616	PS1J1832+6936	PS1J1817+5830	PS1J1809+6036	PS1J1805+2430

Fig. A.6. continued.

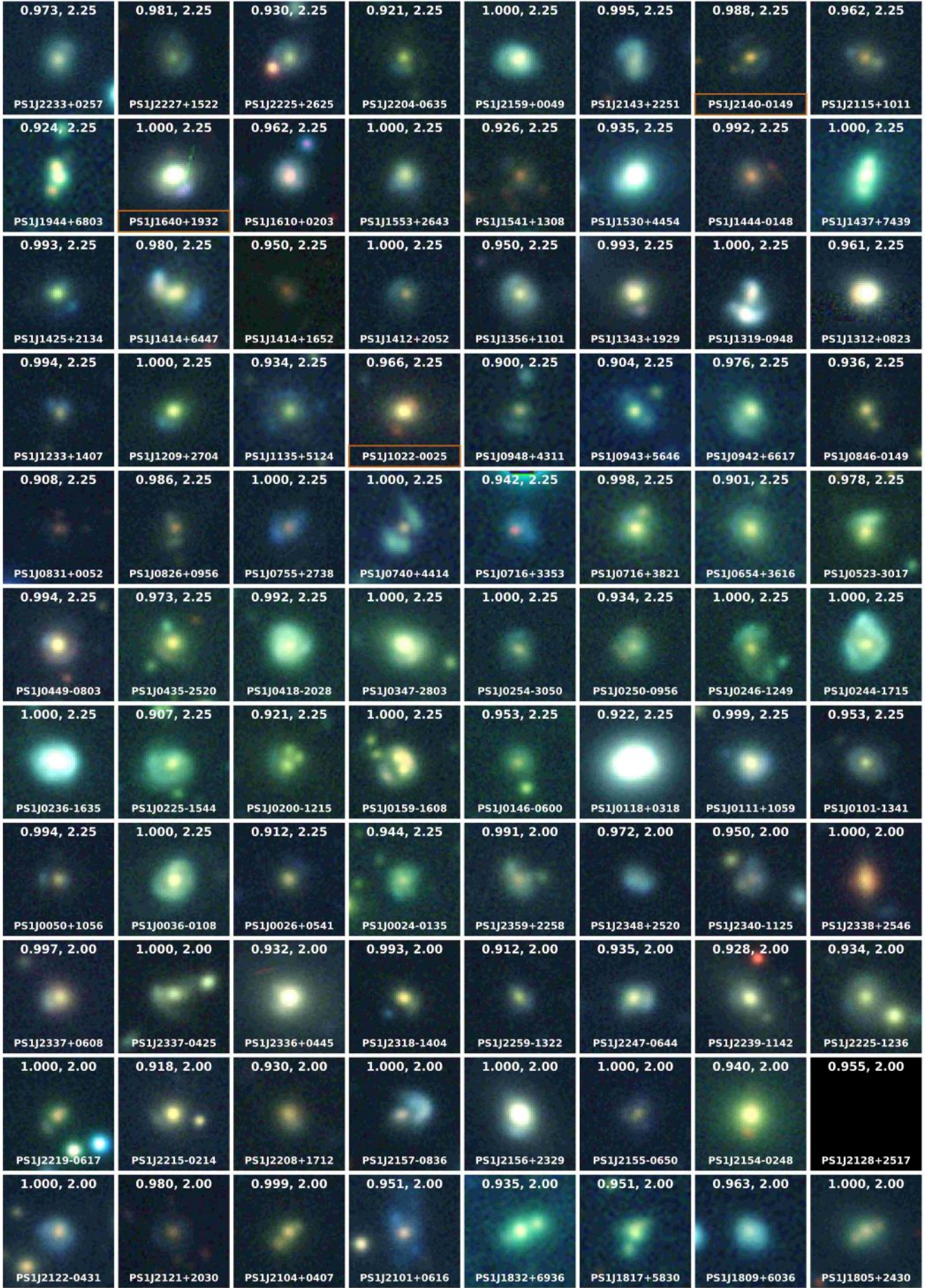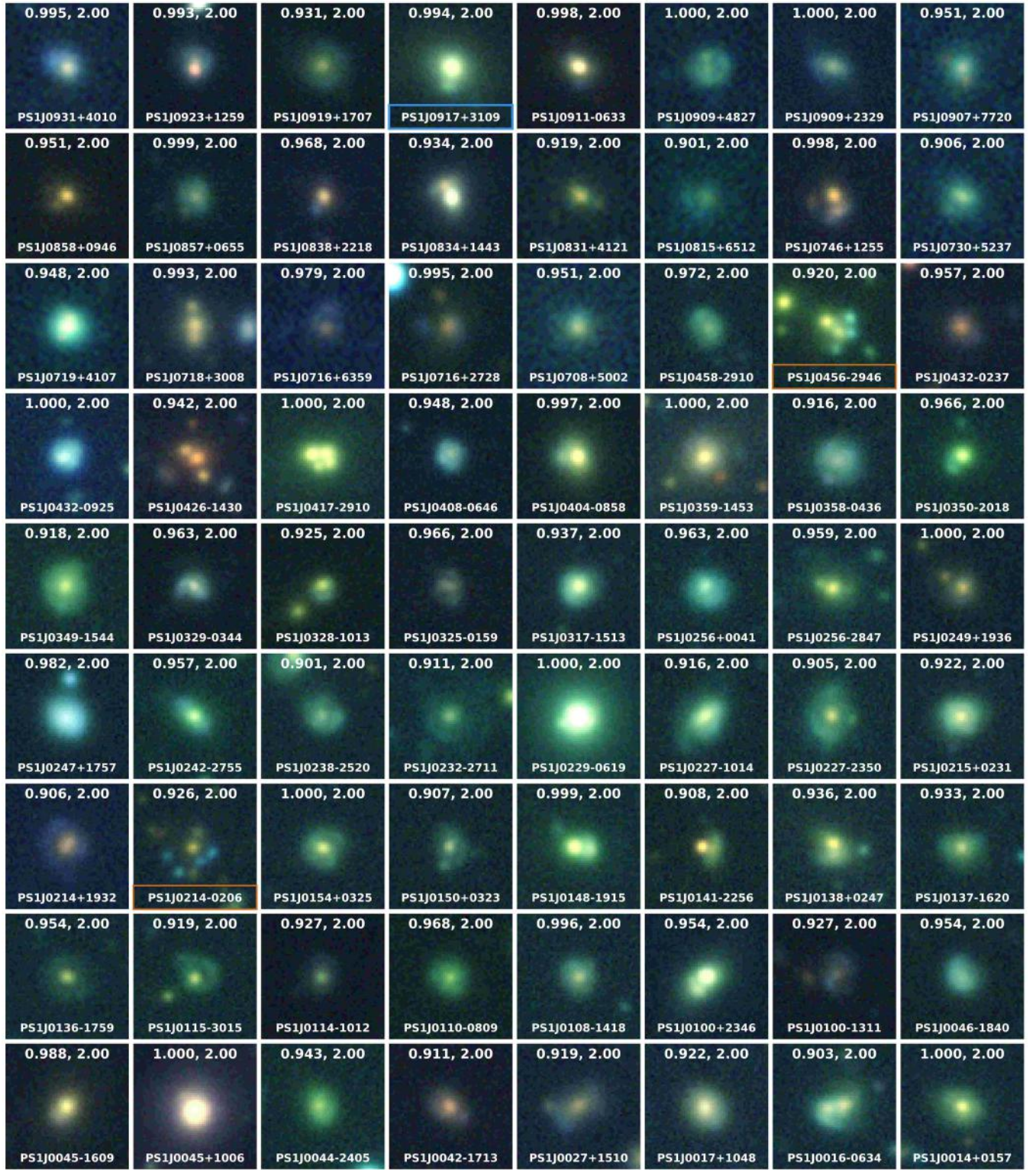|							
0.994, 2.00	1.000, 2.00	1.000, 2.00	0.952, 2.00	0.990, 2.00	1.000, 2.00	0.937, 2.00	0.990, 2.00
PS1J1758+6342	PS1J1757+3631	PS1J1748+3358	PS1J1741+5658	PS1J1730+3405	PS1J1724+3146	PS1J1713+2719	PS1J1705+2849
0.947, 2.00	0.939, 2.00	0.921, 2.00	0.925, 2.00	1.000, 2.00	0.959, 2.00	0.981, 2.00	0.970, 2.00
PS1J1657+2341	PS1J1657+2746	PS1J1649+3049	PS1J1643+3927	PS1J1634+111	PS1J1631+0013	PS1J1625+2224	PS1J1620+5626
0.977, 2.00	0.963, 2.00	0.968, 2.00	1.000, 2.00	0.974, 2.00	0.998, 2.00	1.000, 2.00	0.956, 2.00
PS1J1615+4811	PS1J1613+0146	PS1J1605+1306	PS1J1603+0310	PS1J1558+2429	PS1J1552+4806	PS1J1551+2156	PS1J1548+2156
0.918, 2.00	0.982, 2.00	0.999, 2.00	0.961, 2.00	1.000, 2.00	0.981, 2.00	1.000, 2.00	0.966, 2.00
PS1J1547+0047	PS1J1541+6809	PS1J1539+1425	PS1J1539+1706	PS1J1534+0622	PS1J1501-0330	PS1J1452+1047	PS1J1438+4907
0.966, 2.00	0.919, 2.00	0.988, 2.00	0.905, 2.00	0.968, 2.00	0.946, 2.00	0.998, 2.00	0.944, 2.00
PS1J1436-0223	PS1J1433+0300	PS1J1412-0712	PS1J1412+0432	PS1J1404+4455	PS1J1403-0208	PS1J1355+0011	PS1J1351-0623
0.987, 2.00	0.929, 2.00	0.938, 2.00	1.000, 2.00	0.971, 2.00	0.970, 2.00	0.978, 2.00	0.936, 2.00
PS1J1349-0817	PS1J1341-0247	PS1J1340-0503	PS1J1336+3328	PS1J1327+2926	PS1J1326-0324	PS1J1316+2859	PS1J1315+0104
0.982, 2.00	0.981, 2.00	0.986, 2.00	0.906, 2.00	1.000, 2.00	0.992, 2.00	0.981, 2.00	0.908, 2.00
PS1J1309+0757	PS1J1304+2302	PS1J1301+4123	PS1J1259-0455	PS1J1253-0415	PS1J1244+1802	PS1J1242+0855	PS1J1237+2623
0.977, 2.00	0.964, 2.00	0.937, 2.00	0.999, 2.00	0.987, 2.00	0.991, 2.00	0.956, 2.00	0.992, 2.00
PS1J1221+1406	PS1J1215+1847	PS1J1211+4200	PS1J1206+5302	PS1J1156+5032	PS1J1149+6054	PS1J1148+1347	PS1J1147+2609
0.995, 2.00	0.990, 2.00	0.973, 2.00	0.970, 2.00	1.000, 2.00	0.996, 2.00	1.000, 2.00	0.980, 2.00
PS1J1142+5830	PS1J1139+5252	PS1J1136+1633	PS1J1134+1712	PS1J1132+5436	PS1J1120-0851	PS1J1117+7111	PS1J1108-0143
1.000, 2.00	0.948, 2.00	1.000, 2.00	1.000, 2.00	0.992, 2.00	0.995, 2.00	0.998, 2.00	0.972, 2.00
PS1J1106+1635	PS1J1105+5503	PS1J1104+4118	PS1J1104-0654	PS1J1104-0409	PS1J1101+1822	PS1J1040+3029	PS1J1033+2316
0.987, 2.00	1.000, 2.00	0.912, 2.00	0.999, 2.00	0.921, 2.00	0.958, 2.00	0.991, 2.00	0.966, 2.00
PS1J1028+3820	PS1J1014+3504	PS1J1013+1011	PS1J1001+2133	PS1J0948-0233	PS1J0934-0007	PS1J0933-0247	PS1J0931+2601

Fig. A.7. continued.
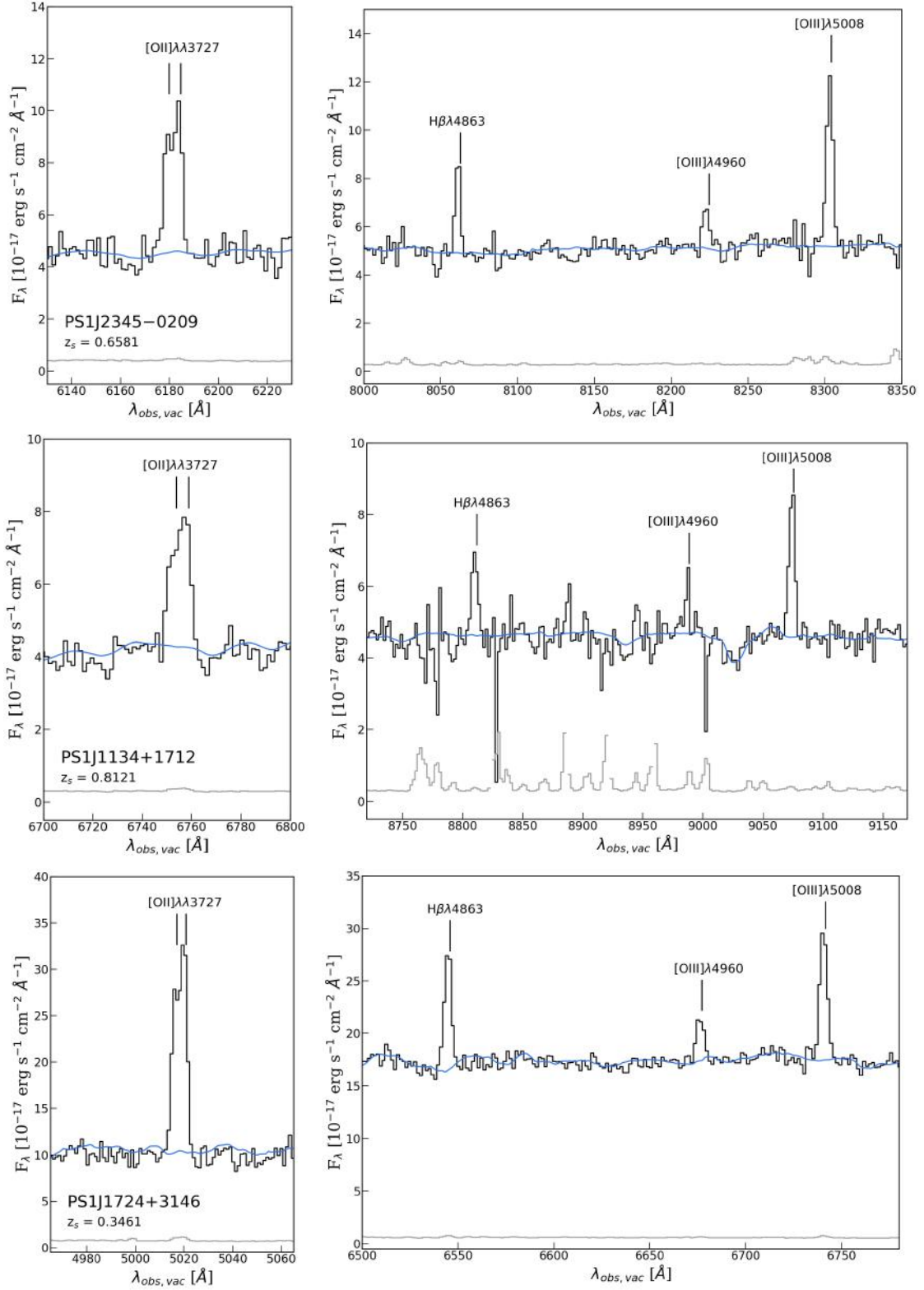
Fig. A.8. continued.

Fig. A.9. PS1 lens candidates with multiple emission lines from a high-redshift background galaxy overlaid on the SDSS BOSS spectrum of the foreground LRG. The black, grey and blue lines show the observed spectrum, the 1σ noise level, and the best-fit SDSS template for the LRG, respectively. The spectrum is zoomed on the spectral features associated with the background line-emitter rather than with the LRG. *Top:* PS1J2345−0209 with $z_{\mathrm{LRG}} = 0.2940$ and $z_{\mathrm{s}} = 0.6581$. *Middle:* PS1J1134+1712 with $z_{\mathrm{LRG}} = 0.3752$ and $z_{\mathrm{s}} = 0.8121$. *Bottom:* PS1J1724+3146 with $z_{\mathrm{LRG}} = 0.2097$ and $z_{\mathrm{s}} = 0.3461$.